Biophysical Journal
Article

Biophysical Society

Light-Activated Dynamic Clamp Using iPSC-Derived Cardiomyocytes

Bonnie Quach,[1,2] Trine Krogh-Madsen,[1,2] Emilia Entcheva,[3] and David J. Christini[1,2,*]
[1]Cardiovascular Research Institute and [2]Weill Cornell Medicine, New York, New York; and [3]Department of Biomedical Engineering, George Washington University, Washington, District of Columbia

ABSTRACT iPSC-derived cardiomyocytes (iPSC-CMs) are a potentially advantageous platform for drug screening because they provide a renewable source of human cardiomyocytes. One obstacle to their implementation is their immature electrophysiology, which reduces relevance to adult arrhythmogenesis. To address this, dynamic clamp is used to inject current representing the insufficient potassium current, I_{K1}, thereby producing more adult-like electrophysiology. However, dynamic clamp requires patch clamp and is therefore low throughput and ill-suited for large-scale drug screening. Here, we use optogenetics to generate such a dynamic-clamp current. The optical dynamic clamp (ODC) uses outward-current-generating opsin, ArchT, to mimic I_{K1}, resulting in more adult-like action potential morphology, similar to I_{K1} injection via classic dynamic clamp. Furthermore, in the presence of an I_{Kr} blocker, ODC revealed expected action potential prolongation and reduced spontaneous excitation. The ODC presented here still requires an electrode to measure V_m but provides a first step toward contactless dynamic clamp, which will not only enable high-throughput screening but may also allow control within multicellular iPSC-CM formats to better recapitulate adult in vivo physiology.

INTRODUCTION

Cardiovascular toxicity is one of the major contributors to drug failure during clinical trials and drug withdrawal from the market (1–4). Improving upon the sensitivity and specificity of preclinical cardiac toxicity assays would greatly mitigate the risk of drug-induced cardiotoxicity to patients and reduce failure of drugs during clinical trials. A limitation of these preclinical tests is that they rely on nonhuman models because human cardiac tissue is a very limited resource. Recent data in multiple areas, including cancer, neurodegenerative diseases, and cardiovascular diseases, indicate that animal models do not recapitulate physiology of human patients faithfully (5–7). The development of human induced pluripotent stem cell-derived cardiomyocytes (iPSC-CMs) offers a promising alternative to nonhuman models by providing a renewable source of human cardiomyocytes. Importantly, iPSC-CMs can be derived from a patient population of interest (8–12).

Despite the advantages of human iPSC-CMs, concerns have been raised about their maturity, which may interfere with predicting the effect of drugs on adult human cardiac function. For example, a low or missing expression of the inward rectifier potassium current, I_{K1}, has been reported as the culprit for spontaneous beating in these cells, considered a sign of immaturity (13–15). I_{K1} is critical for maintaining the resting membrane potential in adult cardiomyocytes and plays a role in late repolarization during an action potential (AP). With insufficient I_{K1}, the resulting phenotype includes more depolarized triangular AP with longer action potential durations (APD). It has been demonstrated that electrically mimicking the low or missing I_{K1} in iPSC-CMs via dynamic clamp, a feedback-control-based electrophysiological technique, can shift the electrophysiological phenotype to more adult-like (15–17). Using this dynamic-clamp approach can help in the study of pro- or anti-arrhythmic effects of drugs on cardiac electrical activity (15). Unlike genetic overexpression of I_{K1}, the electronic expression of an ion channel via the dynamic-clamp method can yield precise dosing and control. The user is able to electrically simulate the presence or absence of a desired current or to interface the patched cell with a mathematical model of another cell to simulate electrotonic interactions and cell behavior in the multicellular setting (15,16,18–20). Dynamic clamp provides high-content electrophysiology data, but its use is limited because of very low throughput and specialized technical expertise. The advent of automated patch clamp with multichannel capabilities works to address some of these barriers to use but is not

Submitted April 19, 2018, and accepted for publication October 2, 2018.
*Correspondence: dchristi@med.cornell.edu
Editor: Henry M. Colecraft.
https://doi.org/10.1016/j.bpj.2018.10.018

without limitations, such as the need for compatibility with cardiomyocytes (currently, it works reliably only with simple non-myocyte cell lines). In an important step in this direction, Goversen et al. (21) recently demonstrated using a Nanion Patchliner automated patch-clamp device to inject I_{K1} via dynamic clamp into iPSC-CMs (21). Here, we present a light-controlled approach to this problem.

Optical methods for stimulation and recording are the natural solution to increasing throughput because their integration permits the parallel interrogation of multiple cells, i.e., the realization of high-throughput all-optical cardiac electrophysiology (22–24). Our long-term goal is to develop a fully optically controlled high-throughput platform that is based on the same principles as dynamic clamp by circumventing the most technical and time-consuming steps of manual patch clamp that are responsible for the low success rate of the method. The optical dynamic clamp (ODC) platform would allow for many more trials because of its noncontact nature and scalability. To realize a fully optically controlled dynamic clamp, we must first establish the use of optogenetic tools to dynamically inject a target current to observe its effect on AP morphology. In subsequent steps, the ODC platform may be adapted to use an optical readout of the membrane potential even though the ODC configuration presented here does require an electrode to measure the membrane potential.

Optogenetic tools are typically used to generate a static current to stimulate APs or completely inhibit electrical activity. An optical AP clamp has been used to uncover the dynamic contribution of Channelrhodopsin-2 (ChR2), a depolarizing opsin, during the cardiac AP (25,26). Several computational (25,27) and experimental studies (28,29) have used depolarizing and hyperpolarizing opsin to modulate the cardiac AP morphology. For example, activation of ChR2 by static light pulses delivered during different AP phases extended the APD in neonatal rat ventricular myocytes (29). Hyperpolarizing anion Channelrhodopsin 1 from *Guillardia theta* (GtACR1) was optically activated by static pulses to shorten the APD in neonatal rat ventricular myocytes via forced hyperpolarization (28). Static optogenetic manipulation can yield a range of AP responses depending on pulse timing, strength, and duration (25); however, it has inherent limitations when applied to multicellular tissue, where cells are at different phases of the AP at any given time. Computationally, a ChR2 model (26) was used to add a dynamic depolarizing current to simulate short QT syndrome and resemble a target AP, yet no real-time feedback was used (27). Although this method worked well in silico, it would be critical to incorporate a real-time feedback loop to address inherent cell variability and make the approach AP-morphology adaptive.

In this study, to demonstrate the use of optogenetics to dynamically tune an AP, we used Archaerhodopsin TP009 (ArchT) (30,31) to optically generate the target outward current I_{K1} instead of using electronic current injection via a patch electrode. ArchT has proven to be a useful tool to inhibit electrical activity in different excitable cells (31–36). To actualize the real-time feedback loop, the optogenetic tool must have fast kinetics and generate sufficient current. For validation purposes, we compared the use of the ODC platform with the standard electrode-based dynamic clamp (EDC) platform to generate a target current mimicking I_{K1} in human iPSC-CMs. We also investigated whether ODC would be able to uncover, as EDC would, the effects of the hERG channel inhibitor E-4031 to illustrate ODC applicability to detect the effect of pharmacological agents on electrical activity. Our experiments demonstrate that ArchT can be controlled to generate the target current and yielded results similar to that of using an electrode even in the presence of an ion channel modulator, corroborating the utility of optogenetic tools in the dynamic clamp setting and in drug-testing applications.

METHODS

Cell culture

Cor.4U human iPSC-CMs (Axiogenesis, Cologne, Germany) were thawed, seeded, and maintained according to the protocols provided by the manufacturer. The cells were seeded on 0.1% gelatin-coated 8 mm coverslips and plated at 100,000 cells/mL. Cells were incubated for at least 7 days post thaw before use for experiments.

Infection and expression of ArchT

Adenoviral vector was constructed using the Addgene (Cambridge, MA) plasmid pAAV-CAG-ArchT-GFP, deposited by K. Deisseroth's laboratory (plasmid 20940) (37,38). ArchT was expressed in iPSC-CMs using multiplicities of infection of 250–300, as described in previously published protocols using an adenovirus (37,38). Determination of successful infection was confirmed via eGFP (enhanced green fluorescent protein) (Fig. S1). Functionality of ArchT was confirmed by illuminating the cells with a light-emitting diode (LED) (M565L3; ThorLabs, Newton, NJ) at 595 nm through a 60× objective and observing the amount of hyperpolarization of the membrane potential under current clamp. Stability of I_{ArchT} was measured with a voltage and light clamp protocol over time to investigate rundown with ArchT illumination (Fig. S12).

Electrophysiology

Borosilicate glass pipettes were pulled to a resistance of 1–3 MΩ using a flaming/brown micropipette puller (Model P-1000; Sutter Instrument, Novato, CA). The pipettes were filled with intracellular solution containing 10 mM NaCl, 130 mM KCl, 1 mM $MgCl_2$, 10 mM $CaCl_2$, 5.5 mM dextrose, 10 mM HEPES. For perforated patch, the pipette tip was first dipped into the intracellular solution without gramicidin for 10 s. The pipette was then filled with the intracellular solution containing 8 μg/mL gramicidin passed through a 0.25 μm filter. The high calcium concentration in the intracellular pipette solution serves to verify the integrity of the patch because patch rupture under these conditions would lead to immediate cell contracture (39). The coverslips containing iPSC-CMs were placed in the bath and constantly perfused with an extracellular solution at 37°C containing 137 mM NaCl, 5.4 mM KCl, 1 mM $MgSO_4$, 2 mM $CaCl_2$, 10 mM dextrose, 10 mM HEPES. GFP-expressing single cells that were visibly contracting were chosen for experiments. Patch-clamp measurements were made by a patch-clamp amplifier (Model 2400; A-M Systems, Sequim, WA) controlled by the Real Time eXperiment Interface (RTXI; http://rtxi.org)

to coordinate the amplifier via the data acquisition card (PCI-6025E; National Instruments, Austin, TX). RTXI was also used to control the LED light intensity. The voltage was corrected for the calculated liquid junction potential of −2.8 mV. The series resistance was less than 10 MΩ and was not compensated.

Dynamic-clamp experiments

Fig. 1 *A* depicts the schematic of the EDC system. At each time step, the electrode measures the membrane potential (V_m), which is then input into a mathematical model of I_{K1} to determine the amount of target current (I_{target}) that should be generated at that measured V_m. The amplifier outputs the calculated I_{target} in real time, simulating the expression of an equivalent current within the cell.

Fig. 1 *B* illustrates the ODC system. Similar to the EDC system, the membrane potential measured by an electrode is input into the mathematical model of the target current. We used the I_{K1} equations of the human ventricular myocyte model by ten Tusscher et al. (40). The maximal allowable I_{target} was set to 1.08 pA/pF because that was close to the maximal current that could be generated by ArchT in these cells. ArchT is a proton pump, generating a light- and voltage-sensitive outward current. There is no published validated mathematical model for the ArchT ion current. Instead, we used an empirical equation that was tuned on a per-cell basis to generate the illumination E_e needed to achieve the target current, I_{ArchT}:

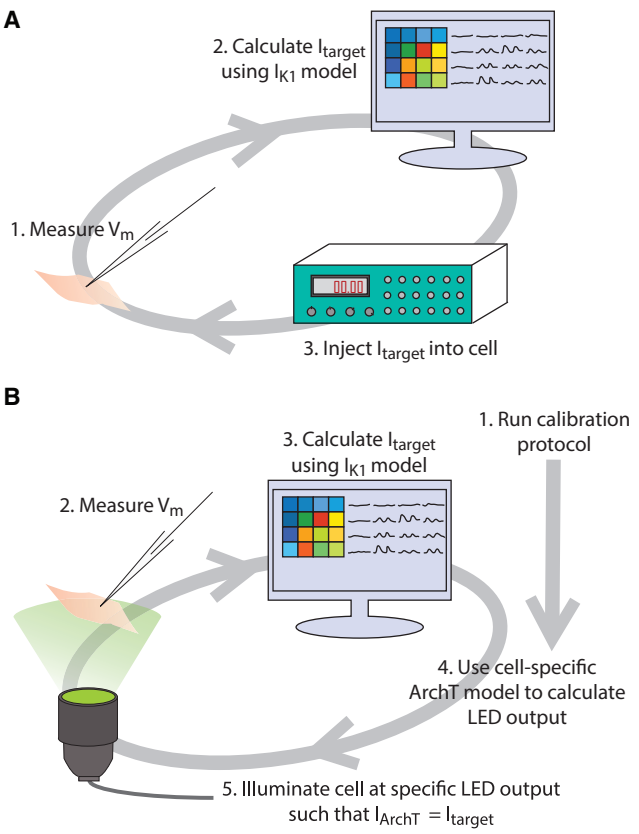

FIGURE 1 Description of EDC and ODC systems. Dynamic clamp is used to simulate the target current, I_{K1}, in iPSC-CMs. (*A*) The EDC system uses the electrode to measure the V_m and inject a current into the cell. (*B*) The ODC system utilizes the electrode to measure the V_m but uses optical ArchT activation to inject the target current. Before implementing the ODC system, a calibration protocol is executed to obtain the parameters to generate a cell-specific ArchT model.

$$I_{ArchT} = \frac{a_1 \times V_m^* + a_2}{a_1 \times V_{rest} + a_2} \times b_1 \left(1 - e^{-b_2 \times E_e}\right), \quad (1)$$

where the first component describes the voltage dependence, which is linearly affected by the membrane potential, and the second component describes the light-intensity dependence of ArchT (Eq. 1; Fig. 2). Because of an amplifier calibration error, the V_m used in this calculation by RTXI (V_m^*) was later determined to be of 5% smaller amplitude than the real V_m as recorded by the amplifier. This error affects I_{ArchT} equally in the EDC and ODC systems, and simulating its effects in a mathematical iPSC-CM model (41) suggests that it has no significant impact on dynamic-clamp performance (Fig. S10). The parameter V_{rest} is set to −85 mV, the ideal resting membrane potential. E_e represents the light intensity of the LED. a_1 and a_2 describe the cell-specific voltage dependence, whereas b_1 and b_2 describe the cell-specific light intensity dependence. The values of these parameters are determined for each cell with a calibration protocol before running the ODC platform so that the ArchT model represents the characteristics from an individual cell. In about half the cells, inward current events are generated spontaneously even during voltage clamp at −85 mV (Fig. S2). These spontaneous events may obscure the recorded current and thus the determination of the cell-specific ArchT parameters. However, cells in which these disturbances did occur were not associated with a reduction in ODC performance, measured as pre-stimulation potential, fraction of repolarization, and triangulation.

To test the feasibility of using ArchT to inject a target current, stimulated APs under the EDC system were compared to those of the ODC platform at three different pacing frequencies: 0.5, 1, and 2 Hz. The cells were stimulated 10 times at 0.5, 1, and 2 Hz sequentially under three conditions (the order of which was randomized): 1) control, in which no additional current was added; 2) addition of I_{target} with EDC; and 3) and addition of I_{target} with ODC.

E-4031 addition

After the cells had undergone the aforementioned pacing protocol under the same three conditions, 500 nM E-4031 was perfused into the bath containing the coverslip of iPSC-CMs for 2 min. Experiments were again conducted under the same pacing protocol and conditions to measure the effect of I_{Kr} inhibition.

Analysis

APD_X was calculated by determining the time from stimulus to the time point at which the AP repolarized X% of the AP amplitude (calculated as AP peak − pre-stimulation potential). The AP peak was defined as the maximal membrane potential reached during the AP after delivered stimulus. The prestimulus potential is defined as an average of the membrane potential in the last 50 ms before delivering a stimulus current. The fraction of repolarization (calculated as $(APD_{90} - APD_{50})/APD_{90}$) and triangulation (calculated as $APD_{90} - APD_{30}$) were used as metrics to quantify AP morphology. Data measured at a given pacing frequency in a cell were omitted from the analysis of AP characteristics if they contained more than one spontaneous event under EDC or ODC. This exclusion was necessary because spontaneous activity could affect the subsequent stimulated AP, obscuring the comparison between EDC and ODC.

RESULTS

Cell-specific calibration

Intrinsic cell-to-cell variability of ArchT expression and characteristics necessitated a calibration protocol that determines the cell-specific parameters of the I_{ArchT} model

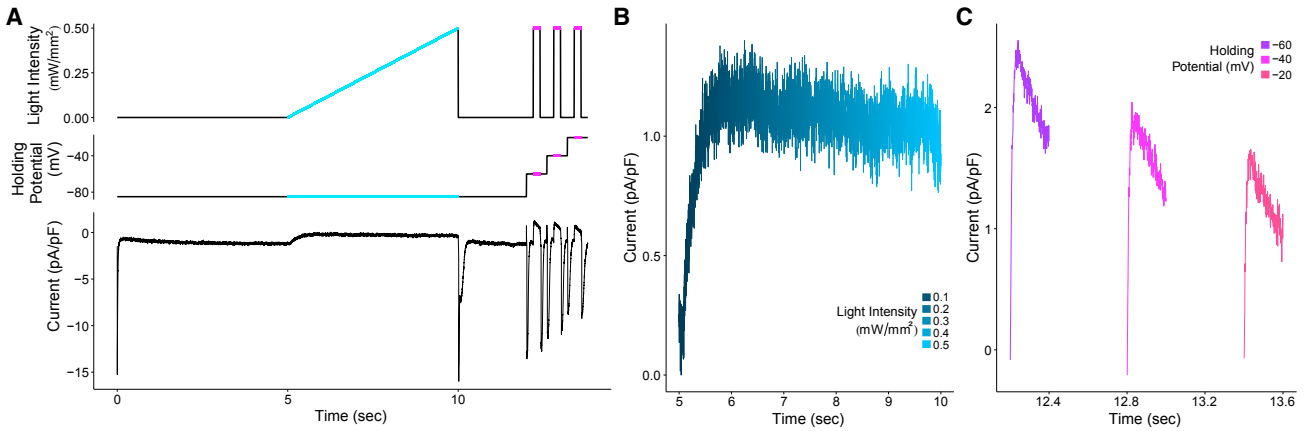

FIGURE 2 Calibration protocol to create a cell-specific ArchT model. (*A*) The calibration protocol consists of changing the light intensity and the holding potential to determine the ArchT model parameters for an individual cell, specifically the light dependence using the light-intensity ramp portion of the protocol (illustrated in *blue*) and voltage dependence using the voltage-clamp steps in the protocol (illustrated in *purple*). The bottom panel illustrates an example of the current output measured via patch clamp for one cell during the calibration protocol. (*B* and *C*) Currents from the example trace in (*A*) during the light-intensity ramp and voltage-clamp steps, respectively, are shown. The currents were subtracted from the baseline, defined as an average of 10 ms before illumination.

(Eq. 1). The calibration protocol consists of a voltage-clamp protocol and a light-clamp protocol (Fig. 2 *A*). The light intensity ramp of the protocol highlighted in blue is used to determine the parameters describing light dependence of I_{ArchT}, whereas the voltage steps highlighted in purple are used to obtain the parameters quantifying its voltage dependence. Fig. 2 *B* depicts the example current trace during the light-intensity ramp on an extended time axis, and Fig. 2 *C* shows the current during each of the three voltage clamp steps. These data are used to obtain the cell-specific parameters by determining the best-fit line using a nonlinear least squares analysis. By deriving the cell-specific ArchT parameters, the light intensity can be accurately calculated to activate ArchT and generate the target current in individual cells.

ODC achieves results similar to EDC

After obtaining the cell-specific parameters for Eq. 1, we then used the ODC method and evaluated its performance compared to EDC. Results from one representative cell paced at 0.5, 1, and 2 Hz are illustrated in Fig. 3. The control yielded a lot of spontaneous activity, making it difficult to trigger a stimulated AP or skewing the subsequent stimulated AP. The EDC and ODC platforms hyperpolarize the membrane potential and inhibit the occurrence of spontaneous events. The stimulated APs in the EDC and ODC conditions are very similar, demonstrating that the EDC and ODC platforms yield nearly identical stimulated APs at different pacing frequencies despite their fundamentally different methods of injecting a current. The EDC target current also overlaps with the ODC target current, as would be expected to generate similar APs. Similar to I_{K1}, the target current is on between APs to maintain the resting membrane potential. During the early phases of the AP, the target current turns off and then increases during repolarization, as I_{K1} would behave. These results indicate that the ODC platform is able to calculate a target current, determine the light intensity needed to generate that target current, adjust the LED output, activate the optical tool, and successfully generate the target current. In short, it demonstrates the feasibility of ArchT to inject a target current analogous to injection via an electrode.

Although the cell presented in Fig. 3 is representative of the most common ODC performance (11 of 16 cells with similar results), in a subset of cells (5 of 16), ODC was unable to maintain the resting membrane potential as well as EDC so that there is a greater than 5 mV difference in the pre-stimulation potential between EDC and ODC. Fig. 4 shows a cell that illustrates this behavior. The gradual depolarizing drift of the ODC membrane potential led to an increase in the target current (and therefore light intensity) as the ODC attempted to hyperpolarize the membrane potential. Although the light intensity did increase, the membrane potential could not be maintained, potentially because ArchT did not generate the required target current. Despite the difference in the pre-stimulation potential, both dynamic-clamp systems had a similar effect on the overall morphology of the stimulated APs, which can be seen by the degree of overlap of the EDC and ODC AP traces. EDC and ODC both inhibited spontaneous activity similarly to the cell in Fig. 3, allowing for better measurement of the AP waveform, whereas without outpacing the intrinsic spontaneous rate, it was difficult under the control condition to measure an AP without a preceding spontaneous event.

Fig. 5 summarizes the effect of EDC and ODC across 16 individual cells on the pre-stimulation potential (Fig. 5 *A*), triangulation (Fig. 5 *B*), and the fraction of repolarization

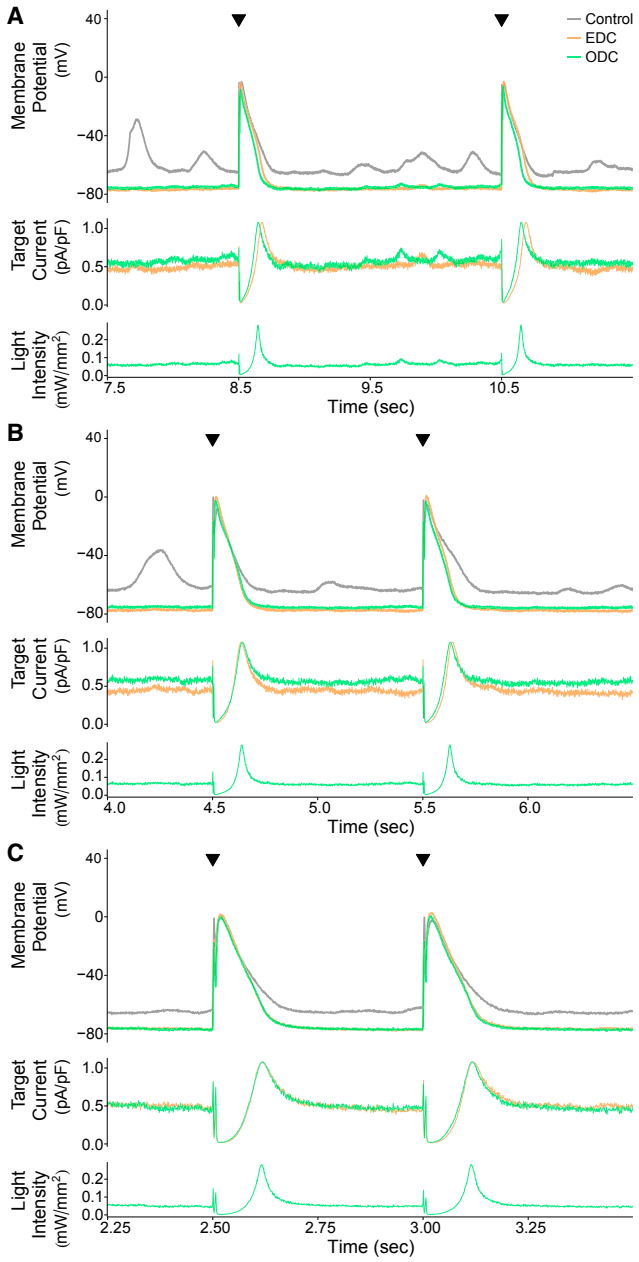

FIGURE 3 Example demonstrating the results of the EDC and ODC platforms. Two stimulated APs from an example cell (cell 1, Figs. S6 *A* and S8) showing the effects of adding I_{target} (I_{K1}) are shown while paced at three different frequencies: (*A*) 0.5 Hz, (*B*) 1 Hz, and (*C*) 2 Hz. The gray, orange, and green traces represent the control without any current addition, adding I_{target} with EDC, and adding I_{target} with ODC, respectively. The top panels in each of (*A*) through (*C*) overlay the paced APs over time under control and both dynamic-clamp conditions, and the black triangles indicate when a stimulus current was delivered. In the middle panels, the traces represent the calculated target currents for EDC and ODC. The bottom panels show the calculated light intensity used to generate the target current. The time axis corresponds to the time within the full recording shown in Fig. S6 *A*.

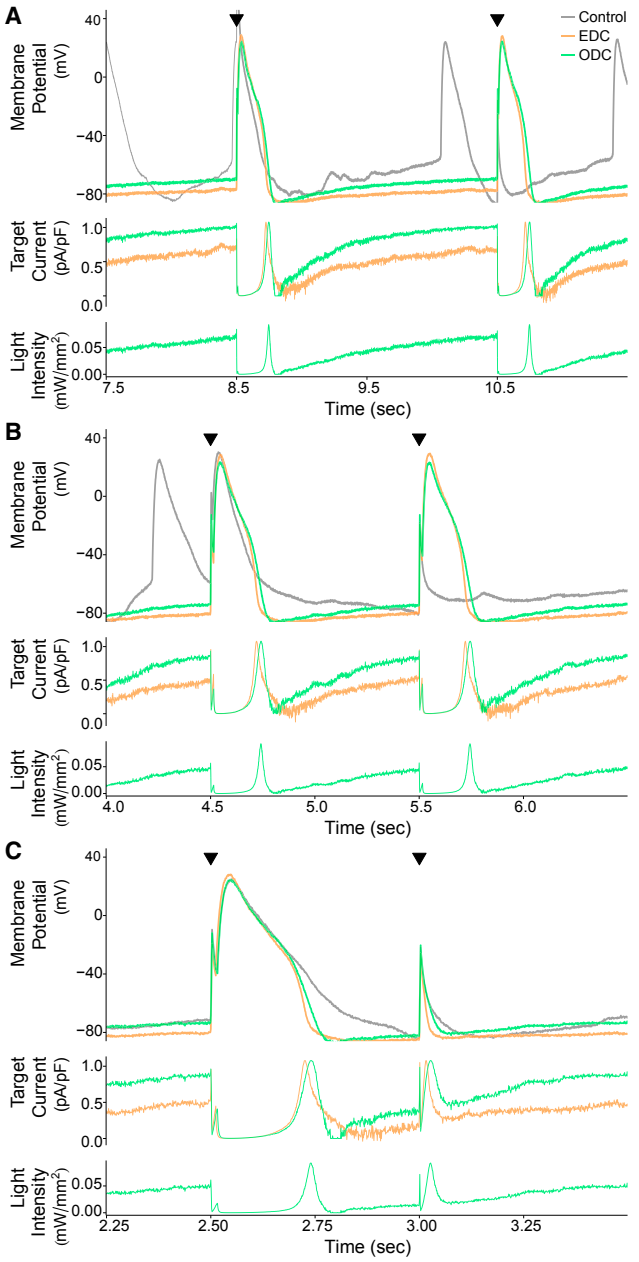

FIGURE 4 Example demonstrating the results of the EDC and ODC platforms. The figure is organized in the same manner as Fig. 3. This example is from cell 13 (Figs. S6 *B* and S8). The time axis corresponds to the time within the full recording shown in Fig. S6 *B*.

(Fig. 5 *C*). EDC and ODC have the advantage over the control condition of suppressing the rate of spontaneous activity, especially when the pacing rate is less than the intrinsic rate (Fig. S3). Both dynamic-clamp systems hyperpolarize the pre-stimulation potential compared to the control (Fig. 5 *A*). Ideally, we would expect ODC to hyperpolarize the pre-stimulation potential to the same value as EDC. In 11 of 16 cells (e.g., the cell in Fig. 3), the pre-stimulation potential in both ODC and EDC were within 5 mV of each other. However, as mentioned above, in 5 of 16 cases (e.g., the cell in Fig. 4), the pre-stimulation potential of the ODC was depolarized more than 5 mV relative to EDC because ODC did not maintain the membrane potential

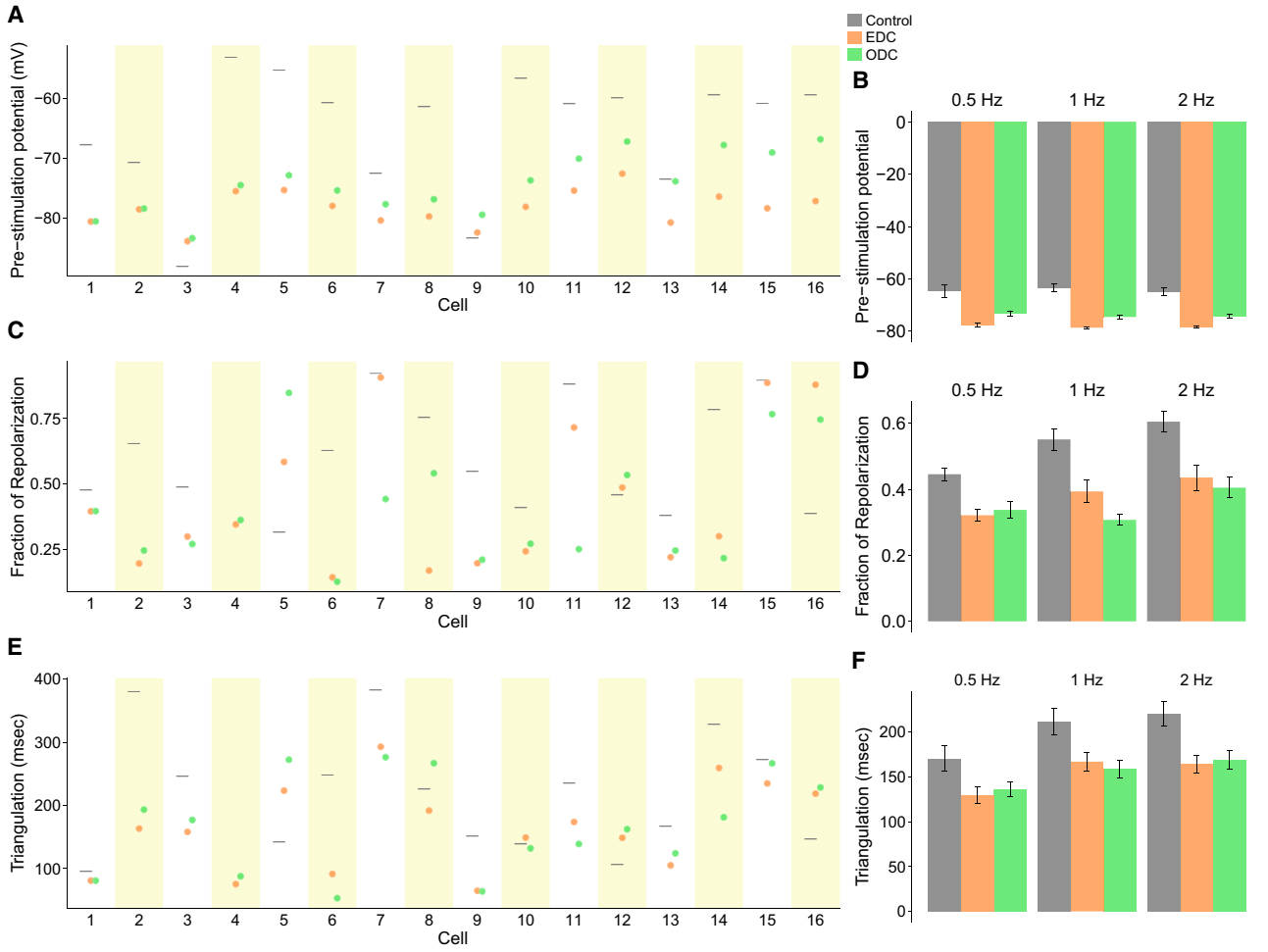

FIGURE 5 Summary of the effects of EDC or ODC on AP morphology. Pre-stimulation potential (*A*), fraction of repolarization (*C*), and triangulation (*E*) of individual cells are shown at 2 Hz pacing in control (*gray*) and after adding an I_{K1} target current via EDC (*orange*) or ODC (*green*). The results of individual cells at 0.5 and 1 Hz are displayed in Fig. S8. Average of all cells and mean ± standard error of the pre-stimulation potential (*B*), fraction of repolarization (*D*), and triangulation (*E*) are shown by pacing frequency; no stimulated AP could be measured for the control condition of cell 16 because of the high rate of spontaneous activity.

as well as EDC did. This is reflected when comparing the average pre-stimulation potentials across conditions (Fig. 5 *D*). Despite the more depolarized pre-stimulation potential, ODC had similar effects as EDC on the overall AP morphology. As one marker of AP morphology, we used fraction of repolarization, which quantifies the fraction of the AP that is spent in the repolarization phase. We expect the fraction of repolarization to decrease with dynamic clamp, given that I_{K1} contributes to late repolarization. The ODC affected the fraction of repolarization by the same magnitude as EDC on average (Fig. 5 *D*), and this is also seen on an individual basis (Fig. 5 *C*). Triangulation provides another marker of the overall shape of the AP. In most cells, ODC altered triangulation by similar magnitudes as EDC (Fig. 5 *E*). The overall average across all pacing frequencies also demonstrates that ODC had a similar effect on triangulation as EDC (Fig. 5 *F*). Additional AP characteristics are provided in Table S1. In summary, comparing the AP characteristics under EDC and ODC reaffirms that ArchT is able to recapitulate similar effects as an electrode on AP morphology.

ODC platform detects effect of I_{Kr} inhibition similar to EDC

To investigate the feasibility of using the ODC platform for drug screening, it is important to determine if ODC can detect changes in AP morphology similar to EDC in the presence of an ion-channel modulator. We used an I_{Kr} inhibitor, E-4031, because I_{Kr} is a dominant repolarizing current in iPSC-CMs and I_{Kr} inhibition assays are commonly used as drug toxicity assays. Fig. 6 shows an example after E-4031 treatment, demonstrating that the ODC platform mimics the effects of EDC on AP morphology. With E-4031 addition, the APD increases in the control, EDC and ODC conditions, as expected with I_{Kr} inhibition

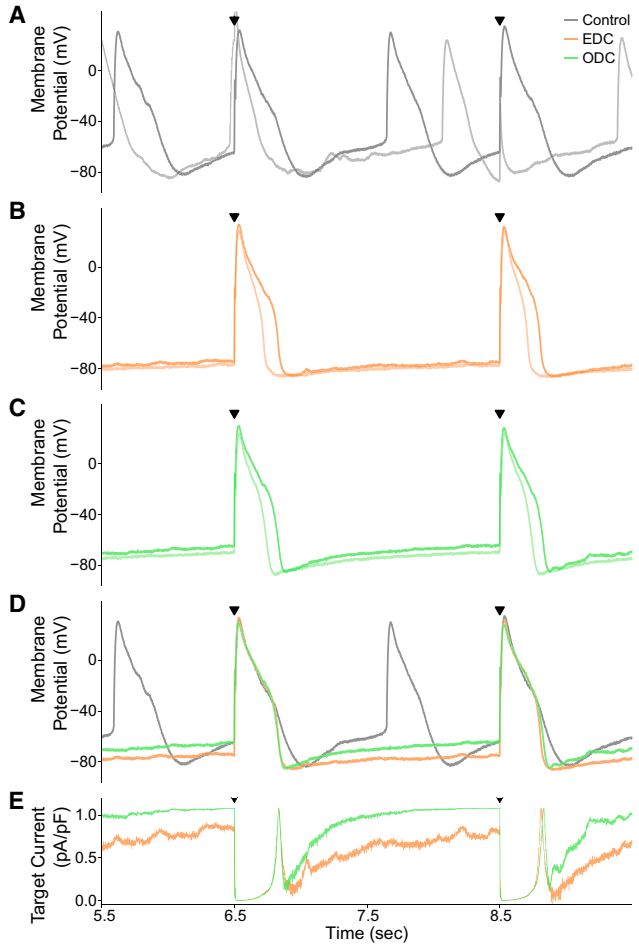

FIGURE 6 Example demonstrating the results of control, EDC, and ODC after E-4031 addition. An example cell (cell 13, Fig. 7) showing the effects of adding I_{target} while paced at 0.5 Hz is shown. The gray (*A* and *D*), orange (*B*, *D*, and *E*), and green (*C*–*E*) traces represent the control without any current addition, adding I_{target} with EDC, and adding I_{target} with ODC, respectively. (*A*–*C*) The darker traces represent the stimulated APs after E-4031 addition, whereas the light-colored traces represent the stimulated APs before E-4031 addition. (*D*) Overlays of AP traces from the three conditions after E-4031 addition are shown. (*E*) Calculated target currents for EDC and ODC are shown. Black triangles indicate when a stimulus current was delivered and provide a reference to which of the 10 paced APs in Fig. S9 are displayed. The time axis corresponds to the time within the full recording shown in Fig. S9.

(Fig. 6, *A*–*C*). Importantly, it is easier to observe the E-4031-induced AP prolongation under EDC and ODC compared to the control because there is less spontaneous activity (Fig. 6, *A*–*C*). That said, like in Fig. 4, ODC does not maintain the membrane potential as well as EDC between APs, which can be seen in the different pre-stimulation potentials (and non-overlapping target currents) (Fig. 6 *D*). However, the overlapping EDC and ODC stimulated APs and target currents during the AP indicate that ArchT achieved a similar effect as the electrode on AP morphology even if the same pre-stimulation potential was not achieved (Fig. 6, *D* and *E*). Thus, the ODC platform behaves like EDC in illuminating the expected changes on AP morphology and APD prolongation with E-4031 addition.

The effect of E-4031 with EDC and ODC across all cells is depicted in Fig. 7. In all cells, EDC and ODC were able to inhibit spontaneous activity seen in the absence of dynamic clamp, allowing for an accurate measurement of AP characteristics. E-4031 increased the APD_{90} under control, EDC, and ODC conditions, as expected (Fig. 7 *A*). Addition of simulated I_{K1} via both dynamic-clamp platforms shortened the APD_{90} compared to the control, as expected with increased repolarizing current. ODC also shortened the APD_{90} to the same magnitude as EDC in individual cells and on average across all cells (Fig. 7, *A* and *E*). Cell 13 under the control condition, yielded too much spontaneous activity after drug addition so that pacing did not override the intrinsic activity to yield stimulated APs. Similar to previous results without E-4031, the effect of ODC and EDC on pre-stimulation potential, fraction of repolarization, and triangulation compared to the control are similar (Fig. 7, *B*–*D*). The average of characteristics across all cells confirm the overall AP morphology (APD_{90}, fraction of repolarization, and triangulation) is nearly identical between EDC and ODC (Fig. 7 *H*). Of note, with E-4031, the control (without dynamic clamp) cells exhibited more dramatic drug-induced effects in terms of APD prolongation and larger triangulation compared to EDC and ODC, which likely indicates that in lack of sufficient I_{K1}, the iPSC-CMs may be overly sensitive to classic hERG channel blockers. The agreement between the ODC and EDC in the presence of E-4031 illustrates how ArchT can be used in place of an electrode in the context of drug screening.

DISCUSSION

ODC performance and limitations

Dynamic clamp is a technique that enables versatile and thorough probing of electrophysiology. However, its use for drug screening is limited because its standard implementation is low throughput. An optically-controlled version would enable more high-throughput applications. Here, we have conducted proof-of-concept experiments in which the light-sensitive hyperpolarizing ion channel ArchT was controlled optically to inject I_{K1}-like target current and to alter AP morphology similarly to electrode-based dynamic clamp. Our findings demonstrate 1) the feasibility of using optogenetics to generate a dynamically controlled target current and 2) the potential of the ODC platform to be used for drug screening in place of EDC.

Compared to EDC, ODC displayed decreased ability to maintain a hyperpolarized membrane potential between APs in some cells. The resulting differences in pre-stimulation potential could conceivably cause secondary changes in AP features. However, this possibility was ruled out because there was no correlation between the difference in

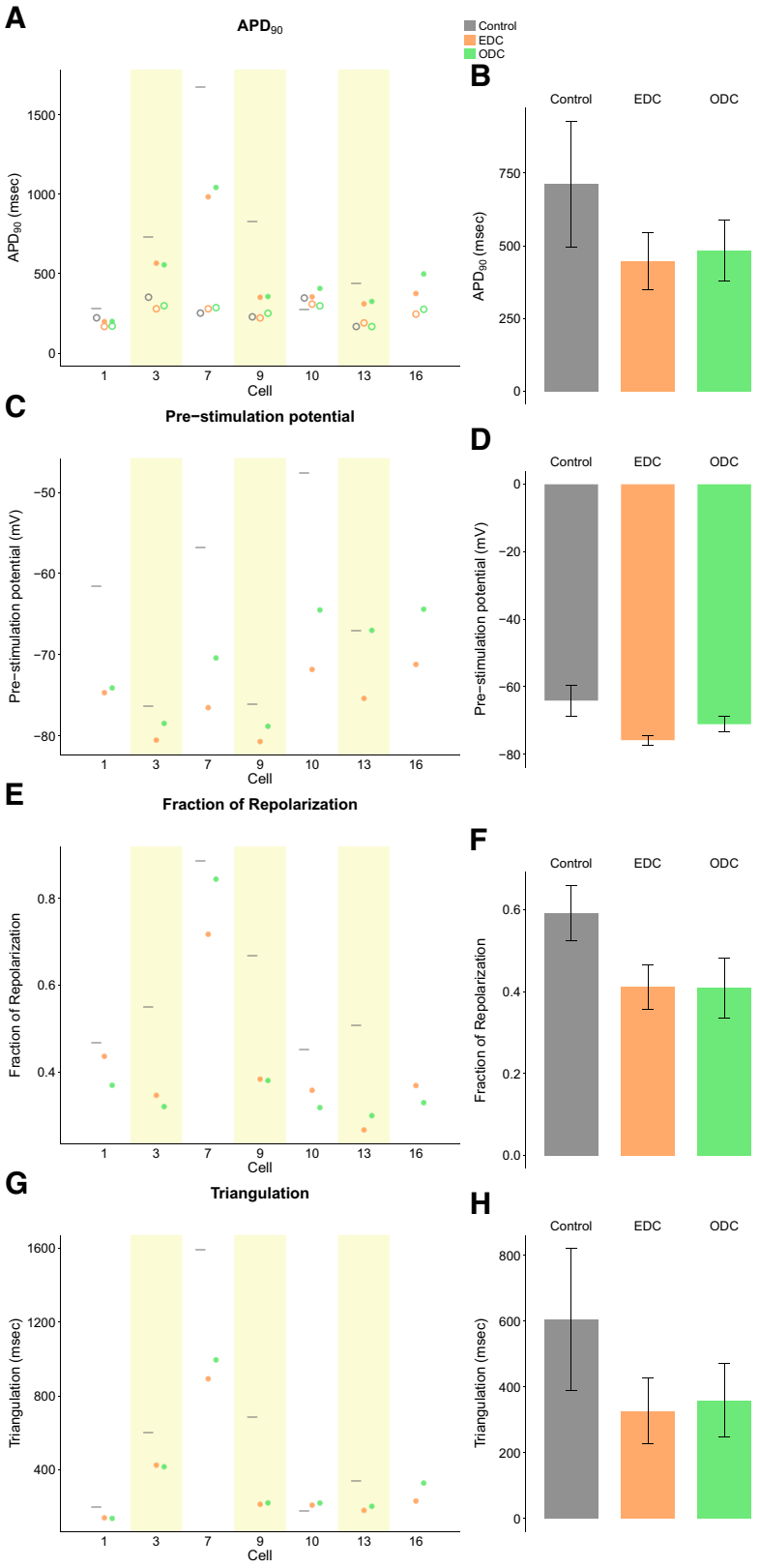

FIGURE 7 Summary of the effect of adding I_{K1} via EDC or ODC after E-4031 addition on AP morphology paced at 0.5 Hz. The APD_{90} (*A*), pre-stimulation potential (*C*), fraction of repolarization (*E*), and triangulation (*G*) were measured without any current addition (*gray*) and with the addition of I_{target} via EDC (*orange*) or ODC (*green*) in individual cells. (*A*) The empty markers represent the APD_{90} before drug addition, and the dark circles represent the APD_{90} after E-4031 addition. The average of all cells and mean ± standard error of the APD_{90} after drug addition (*B*), pre-stimulation potential (*D*), fraction of repolarization (*F*), and triangulation (*H*) are shown.

pre-stimulation potential between EDC and ODC on the differences of fraction of repolarization and triangulation (Fig. S4). One explanation for the inability of ArchT to maintain a hyperpolarized membrane potential as well as EDC does is the relatively low maximal current that a light-driven ion pump can generate. Indeed, ArchT pushes

one H^+ ion per photon, which is much less efficient than the operation of a light-sensitive ion channel. Furthermore, the ArchT current seemed to decay during the voltage-dependence part of the calibration protocol (Fig. 2 *C*). During the intervals between APs, such ArchT current decay could depolarize the membrane. We tested this hypothesis by quantifying the correlation between the cell-specific current decay and the difference between the pre-stimulation potentials between EDC and ODC (Fig. S5). No such correlation was found, suggesting that it is unlikely that the current decay is responsible for the lack of V_m maintenance.

Another potential limitation of ODC is that because ArchT is a proton pump, there may be a pH effect. Archaerhodopsins themselves are known to be pH sensitive, so a local change in pH could affect the ability of ArchT to generate a consistent current (42–44). Local changes in pH could affect neighboring ion channels directly or indirectly by affecting the membrane and altering the overall electrophysiological properties of the cell (44–47). The observation that ODC inhibited spontaneous activity more effectively than EDC (Fig. S3) may be evidence of this effect on other ion channels either by directly affecting the structure of the proximal channels or indirectly by altering the surrounding membrane properties. The increased inhibition of spontaneous activity with ODC can serve as an advantage over EDC because AP morphology can be measured without any distortion from underlying spontaneous events.

In some cells, we observed a voltage undershoot after the AP (Figs. 4 and S4) (8,13,15,48–56). The magnitude of this undershoot varied across cells. EDC was better able to inhibit this undershoot by injecting a depolarizing current (Fig. S4); not surprisingly, the hyperpolarizing opsin was not helpful in correcting this feature. The cause and consequences of this undershoot are not fully understood but can account for the differences between the ODC and EDC and explain why in some cases, the AP morphology with ODC looks more like the control than EDC (Fig. S7). The increased hyperpolarization seen in control and ODC conditions may have consequences for the subsequent AP by altering the activation state of other ion channels. Extension of the ODC method to incorporate a depolarizing opsin would allow bidirectional voltage control and thereby compensate for the undershoot, similar to EDC. Indeed, this would allow the ODC to mimic any electrical current and thereby be fully versatile like EDC. Finally, there are limitations to our empirical approach to modeling ArchT as an on/off light switch in Eq. 1. Taking into account the ArchT's intermediate states of different conductance (30,57) and developing more mechanistic models, as done for ChR2 (26), may help improve similarity between EDC and ODC. This will allow for better control of light levels and more precise generation of the predicted current.

The maximal I_{target} of 1.08 pA/pF used in our study was determined based on the maximal current that could be consistently generated by the genetically expressed ArchT in the voltage range relevant to I_{K1}. The I_{target} generated during our dynamic-clamp experiments typically reached 1.08 pA/pF during final repolarization (e.g., Fig. 3), and it reached a maximum of around 0.5 pA/pF during rest because of decreased driving force. We expect that a larger I_{target} would allow hyperpolarization to below the −80 mV level as seen in previous studies of EDC (15,16,21), although the maximal current used here falls within the reported range for maximal outward I_{K1} in adult human ventricular myocytes (0.5–2.2 pA/pF) (16).

Dynamic clamp is based on a real-time feedback loop. Because ArchT is not an instantaneous current, it is critical that its kinetics are fast enough for the purposes of dynamic clamp. We investigated the effect of the time constant of activation and deactivation on dynamic-clamp performance in silico (Fig. S11 *A*). The in silico results suggest that for I_{K1}, there is tolerance of the ODC system for a time constant of at least 30 ms before the resulting AP waveform deviates substantially from the control. We measured the time constant in our cells to be less than 15 ms and therefore within the predicted acceptable range (Fig. S11 *B*).

We have yet to eliminate the need for an electrode by incorporating an optical method to measure the membrane potential. To make this platform fully optical, there are several anticipated challenges. Currently available optical methods of measuring membrane potential are voltage-sensitive dyes and other opsins (e.g., QuasAr2, Arch(D95X), and CaViar) (12,58). These options do not quantify the absolute membrane potential as required in this implementation to calculate the target current. Hou et al. (59) reported a method of using the temporal dynamics of microbial rhodopsin fluorescence to measure the absolute membrane potential, but that method is too complex and not compatible with the mechanics of dynamic clamp (59). Ratiometric sensors, combined with proper membrane voltage calibration, can present a path toward absolute voltage measurements. However, experience with ratiometric calcium indicators and attempts to estimate absolute intracellular calcium levels have revealed the many challenges of such methodology. In addition, the generally noisier fluorescent signals may interefere with the I_{target} calculation, possibly affecting the accuracy of the dynamic clamp. Dynamic clamp relies on the real-time feedback of information, so a fully optical dynamic-clamp platform would require a stable and rapidly responsive voltage sensor. Realization of the fully optical dynamic-clamp dream will require development of optical tools that are conducive to dynamic clamp.

Using ODC for drug screening

The tedious nature of dynamic clamp restricts its use, but were it high throughput, it would open the possibility for its use during pre-clinical drug development. To increase throughput, an all-optical system would require an optical

voltage readout, using, e.g., a voltage-sensitive dye or a genetically encoded voltage indicator. The necessary requirements for compatibility in the ODC system would be defined by phototoxicity, brightness, responsiveness, and wavelength crosstalk. One of the biggest advantages of the ODC platform is that it is compatible with a variety of cell formats. In spatially extended systems (e.g., large beating clusters and monolayers), the EDC platform is not applicable, whereas the ODC platform can be used to illuminate the arrhythmogenic effects of drugs. These more tissue-like formats capture "in-context" cell behavior, including electrotonic coupling and other chemical influences from neighboring cells, and therefore are preferred to single cells. Furthermore, all-optical methods enable high-precision space-time control in such multicellular systems, as illustrated recently in neurons (60) and in cardiac preparations (22). This allows users to redirect the control of electrical activity from the single-cell behavior to the emergent (wave) behavior (22,23).

Versatility and flexibility of ODC

With the right optogenetic tools and mathematical models, the ODC platform could open up more physiologically relevant formats for basic science research and drug development. Halorhodopsins such as *Natronomonas pharaonis* halorhodopsin (NpHR) and its derivatives could also be used in this platform as an alternative to ArchT to inject a hyperpolarizing current given their fast kinetics (61). Neither of these generate particularly high current, considering that they are light-sensitive ion pumps. GtACR1 is a Cl^- current with large amplitude (28,62) that is also fast and thus very promising; its utility in adult cardiomyocytes and physiological concentrations remains to be demonstrated. BLINK1 is the first potassium-selective optogenetic tool available, but its kinetics are currently too slow for the near real-time feedback requirements of ODC (63). There are also several depolarizing opsins available that can be used in conjunction with hyperpolarizing opsins so that any inward or outward current can be represented in cardiomyocytes (61,64,65). Optogenetic tools are being engineered to activate/deactivate faster, generate larger photocurrents, be permeable to specific ionic species, or be activated by specific wavelengths. As these developments progress, users can choose which optogenetic tool best suits their needs in the ODC platform.

One known drawback of EDC is that an electrode can only electrically mimic a current but cannot account for endogenous secondary effects that affect electrophysiology, such as activation of exchangers, pumps, or Ca^{2+}-dependent processes, which typically result from the change in intracellular ionic concentration. In this regard, because optogenetic tools alter the membrane potential by changing the intracellular ionic composition, the ODC platform may be more suitable for dynamic clamp than using an electrode because optogenetics can generate a custom-tailored current with the intended ionic species itself, reflecting how endogenous currents are generated. As with the standard dynamic-clamp method, ArchT mimicked the electrical behavior of I_{K1}. But as potassium-selective tools are made compatible with the dynamic-clamp system, the ODC platform may recapitulate both the electrical effect of I_{K1} and its effects from altering the intracellular potassium concentration. With the expansion of the optogenetic toolbox, the ODC platform will more accurately investigate the true influence of an ionic current on electrophysiological behavior by generating the current with the relevant species.

Optogenetic tools are being creatively incorporated into automated high-throughput drug-screening platforms (12,21,24,66). Using optogenetic tools dynamically could also potentially expand on the use of automated multi-channel patch-clamp systems to multicellular preparations. Such a hybrid system could continue to use a patch electrode to read the V_m but instead use optogenetic methods to inject a dynamic current, which would be required to control all of the cells in the multicellular format. Opsins would be expressed in each cell such that a target current could be generated in each cell in parallel manner, expanding the reach of a pipette, which can only inject a current locally.

The ODC method contributes a novel approach, to our knowledge, to probe electrical dynamics in iPSC-CMs and to better reveal how electrical activity is controlled. Here, a proof-of-principle ODC application was demonstrated with ArchT to generate I_{K1} as target current in iPSC-CMs to simulate a more adult-like electrical phenotype. As the ODC platform develops, it should be possible to simulate abnormal currents or heterogeneous current expression in iPSC-CM monolayers. This would provide a more powerful approach that enables researchers to address hypotheses that could not be investigated previously.

SUPPORTING MATERIAL

Twelve figures and one table are available at http://www.biophysj.org/biophysj/supplemental/S0006-3495(18)31166-4.

AUTHOR CONTRIBUTIONS

B.Q. designed the experiments, conducted experiments, performed analysis, developed models, and wrote the manuscript. T.K.-M. and D.J.C. supervised experimental design, modeling, and analysis. E.E. provided reagents and protocols for the optogenetic actuator. B.Q., T.K.-M., E.E., and D.J.C. reviewed and edited the manuscript.

ACKNOWLEDGMENTS

This work was supported by F31 HL134209-02 to B.Q., the PhRMA Foundation Predoctoral Fellowship to B.Q., National Institutes of Health RO1HL111649 to E.E., and R01EB016407 to D.J.C.

REFERENCES

1. Redfern, W. S., L. Carlsson, …, T. G. Hammond. 2003. Relationships between preclinical cardiac electrophysiology, clinical QT interval prolongation and torsade de pointes for a broad range of drugs: evidence for a provisional safety margin in drug development. *Cardiovasc. Res.* 58:32–45.
2. Stevens, J. L., and T. K. Baker. 2009. The future of drug safety testing: expanding the view and narrowing the focus. *Drug Discov. Today.* 14:162–167.
3. Laverty, H., C. Benson, …, J. Valentin. 2011. How can we improve our understanding of cardiovascular safety liabilities to develop safer medicines? *Br. J. Pharmacol.* 163:675–693.
4. Ferri, N., P. Siegl, …, R. Benghozi. 2013. Drug attrition during preclinical and clinical development: understanding and managing drug-induced cardiotoxicity. *Pharmacol. Ther.* 138:470–484.
5. Mak, I. W., N. Evaniew, and M. Ghert. 2014. Lost in translation: animal models and clinical trials in cancer treatment. *Am. J. Transl. Res.* 6:114–118.
6. Olson, H., G. Betton, …, A. Heller. 2000. Concordance of the toxicity of pharmaceuticals in humans and in animals. *Regul. Toxicol. Pharmacol.* 32:56–67.
7. Scott, S., J. E. Kranz, …, J. A. Heywood. 2008. Design, power, and interpretation of studies in the standard murine model of ALS. *Amyotroph. Lateral Scler.* 9:4–15.
8. Itzhaki, I., L. Maizels, …, L. Gepstein. 2011. Modelling the long QT syndrome with induced pluripotent stem cells. *Nature.* 471:225–229.
9. Guo, L., L. Coyle, …, K. L. Kolaja. 2013. Refining the human iPSC-cardiomyocyte arrhythmic risk assessment model. *Toxicol. Sci.* 136:581–594.
10. Harris, K., M. Aylott, …, A. Sridhar. 2013. Comparison of electrophysiological data from human-induced pluripotent stem cell-derived cardiomyocytes to functional preclinical safety assays. *Toxicol. Sci.* 134:412–426.
11. Sinnecker, D., K. L. Laugwitz, and A. Moretti. 2014. Induced pluripotent stem cell-derived cardiomyocytes for drug development and toxicity testing. *Pharmacol. Ther.* 143:246–252.
12. Dempsey, G. T., K. W. Chaudhary, …, J. M. Kralj. 2016. Cardiotoxicity screening with simultaneous optogenetic pacing, voltage imaging and calcium imaging. *J. Pharmacol. Toxicol. Methods.* 81:240–250.
13. Ma, J., L. Guo, …, C. T. January. 2011. High purity human-induced pluripotent stem cell-derived cardiomyocytes: electrophysiological properties of action potentials and ionic currents. *Am. J. Physiol. Heart Circ. Physiol.* 301:H2006–H2017.
14. Lieu, D. K., J. D. Fu, …, R. A. Li. 2013. Mechanism-based facilitated maturation of human pluripotent stem cell-derived cardiomyocytes. *Circ Arrhythm Electrophysiol.* 6:191–201.
15. Bett, G. C., A. D. Kaplan, …, R. L. Rasmusson. 2013. Electronic "expression" of the inward rectifier in cardiocytes derived from human-induced pluripotent stem cells. *Heart Rhythm.* 10:1903–1910.
16. Meijer van Putten, R. M., I. Mengarelli, …, R. Wilders. 2015. Ion channelopathies in human induced pluripotent stem cell derived cardiomyocytes: a dynamic clamp study with virtual IK1. *Front. Physiol.* 6:7.
17. Verkerk, A. O., C. C. Veerman, …, R. Wilders. 2017. Patch-clamp recording from human induced pluripotent stem cell-derived cardiomyocytes: improving action potential characteristics through dynamic clamp. *Int. J. Mol. Sci.* 18:E1873.
18. Ortega, F. A., R. J. Butera, …, A. D. Dorval, II. 2014. Dynamic clamp in cardiac and neuronal systems using RTXI. *Methods Mol. Biol.* 1183:327–354.
19. Brown, T. R., T. Krogh-Madsen, and D. J. Christini. 2016. Illuminating myocyte-fibroblast homotypic and heterotypic gap junction dynamics using dynamic clamp. *Biophys. J.* 111:785–797.
20. Devenyi, R. A., F. A. Ortega, …, E. A. Sobie. 2017. Differential roles of two delayed rectifier potassium currents in regulation of ventricular action potential duration and arrhythmia susceptibility. *J. Physiol.* 595:2301–2317.
21. Goversen, B., N. Becker, …, T. P. de Boer. 2018. A hybrid model for safety pharmacology on an automated patch clamp platform: using dynamic clamp to join iPSC-derived cardiomyocytes and simulations of I_{k1} ion channels in real-time. *Front. Physiol.* 8:1094.
22. Burton, R. A., A. Klimas, …, G. Bub. 2015. Optical control of excitation waves in cardiac tissue. *Nat. Photonics.* 9:813–816.
23. Entcheva, E., and G. Bub. 2016. All-optical control of cardiac excitation: combined high-resolution optogenetic actuation and optical mapping. *J. Physiol.* 594:2503–2510.
24. Klimas, A., C. M. Ambrosi, …, E. Entcheva. 2016. OptoDyCE as an automated system for high-throughput all-optical dynamic cardiac electrophysiology. *Nat. Commun.* 7:11542.
25. Entcheva, E., and J. C. Williams. 2014. Channelrhodopsin2 current during the action potential: "optical AP clamp" and approximation. *Sci. Rep.* 4:5838.
26. Williams, J. C., J. Xu, …, E. Entcheva. 2013. Computational optogenetics: empirically-derived voltage- and light-sensitive channelrhodopsin-2 model. *PLoS Comput. Biol.* 9:e1003220.
27. Karathanos, T. V., P. M. Boyle, and N. A. Trayanova. 2014. Optogenetics-enabled dynamic modulation of action potential duration in atrial tissue: feasibility of a novel therapeutic approach. *Eurospace.* 16:iv69–iv76.
28. Govorunova, E. G., S. R. Cunha, …, J. L. Spudich. 2016. Anion channelrhodopsins for inhibitory cardiac optogenetics. *Sci. Rep.* 6:33530.
29. Park, S. A., S. R. Lee, …, D. T. Yue. 2014. Optical mapping of optogenetically shaped cardiac action potentials. *Sci. Rep.* 4:6125.
30. Chow, B. Y., X. Han, and E. S. Boyden. 2012. Genetically encoded molecular tools for light-driven silencing of targeted neurons. *Prog. Brain Res.* 196:49–61.
31. Han, X., B. Y. Chow, …, E. S. Boyden. 2011. A high-light sensitivity optical neural silencer: development and application to optogenetic control of non-human primate cortex. *Front. Syst. Neurosci.* 5:18.
32. Huff, M. L., R. L. Miller, …, R. T. LaLumiere. 2013. Posttraining optogenetic manipulations of basolateral amygdala activity modulate consolidation of inhibitory avoidance memory in rats. *Proc. Natl. Acad. Sci. USA.* 110:3597–3602.
33. Nussinovitch, U., R. Shinnawi, and L. Gepstein. 2014. Modulation of cardiac tissue electrophysiological properties with light-sensitive proteins. *Cardiovasc. Res.* 102:176–187.
34. Li, B., X. Y. Yang, …, L.-Y. Chiang. 2015. A novel analgesic approach to optogenetically and specifically inhibit pain transmission using TRPV1 promoter. *Brain Res.* 1609:12–20.
35. Tsunematsu, T., and A. Yamanaka. 2015. Elucidation of neuronal circuitry involved in the regulation of sleep/wakefulness using optogenetics. *In* Optogenetics. H. Yawo, H. Kandori, and A. Koizumi, eds. Springer, pp. 249–263.
36. Lux, V., O. A. Masseck, …, M. M. Sauvage. 2017. Optogenetic destabilization of the memory trace in CA1: insights into reconsolidation and retrieval processes. *Cereb. Cortex.* 27:841–851.
37. Ambrosi, C. M., and E. Entcheva. 2014. Optogenetic control of cardiomyocytes via viral delivery. *Methods Mol. Biol.* 1181:215–228.
38. Yu, J., and E. Entcheva. 2016. Inscribing optical excitability to non-excitable cardiac cells: viral delivery of optogenetic tools in primary cardiac fibroblasts. *Methods Mol. Biol.* 1408:303–317.
39. Ishihara, K., D. H. Yan, …, T. Ehara. 2002. Inward rectifier K(+) current under physiological cytoplasmic conditions in guinea-pig cardiac ventricular cells. *J. Physiol.* 540:831–841.
40. ten Tusscher, K. H., D. Noble, P. J. Noble, and A. V. Panfilov. 2014. A model for human ventricular tissue. *Am. J. Physiol. Heart Circ. Physiol.* 286:H1573–H1589.
41. Paci, M., J. Hyttinen, K. Aalto-Setälä, and S. Severi. 2013. Computational models of ventricular- and atrial-like human induced pluripotent stem cell derived cardiomyocytes. *Ann. Biomed. Eng.* 41:2334–2348.

42. Lukashev, E. P., R. Govindjee, …, Y. Mukohata. 1994. pH dependence of the absorption spectra and photochemical transformations of the archaerhodopsins. *Photochem. Photobiol.* 60:69–75.

43. Ming, M., M. Lu, …, J. Ding. 2006. pH dependence of light-driven proton pumping by an archaerhodopsin from Tibet: comparison with bacteriorhodopsin. *Biophys. J.* 90:3322–3332.

44. Saint Clair, E. C., J. I. Ogren, …, K. J. Rothschild. 2012. Near-IR resonance Raman spectroscopy of archaerhodopsin 3: effects of transmembrane potential. *J. Phys. Chem. B.* 116:14592–14601.

45. Bedlack, R. S., Jr., M. D. Wei, …, L. M. Loew. 1994. Distinct electric potentials in soma and neurite membranes. *Neuron.* 13:1187–1193.

46. Beppu, K., T. Sasaki, …, K. Matsui. 2014. Optogenetic countering of glial acidosis suppresses glial glutamate release and ischemic brain damage. *Neuron.* 81:314–320.

47. El-Gaby, M., Y. Zhang, …, O. A. Shipton. 2016. Archaerhodopsin selectively and reversibly silences synaptic transmission through altered pH. *Cell Rep.* 16:2259–2268.

48. Kato, Y., H. Masumiya, …, K. Shigenobu. 1996. Developmental changes in action potential and membrane currents in fetal, neonatal and adult guinea-pig ventricular myocytes. *J. Mol. Cell. Cardiol.* 28:1515–1522.

49. Caspi, O., I. Itzhaki, …, L. Gepstein. 2009. In vitro electrophysiological drug testing using human embryonic stem cell derived cardiomyocytes. *Stem Cells Dev.* 18:161–172.

50. Haase, A., R. Olmer, …, U. Martin. 2009. Generation of induced pluripotent stem cells from human cord blood. *Cell Stem Cell.* 5:434–441.

51. Moretti, A., M. Bellin, …, K. L. Laugwitz. 2010. Patient-specific induced pluripotent stem-cell models for long-QT syndrome. *N. Engl. J. Med.* 363:1397–1409.

52. Sun, N., M. Yazawa, …, J. C. Wu. 2012. Patient-specific induced pluripotent stem cells as a model for familial dilated cardiomyopathy. *Sci. Transl. Med.* 4:130ra47.

53. Itoh, H. 2013. Electrophysiological simulation of developmental changes in action potentials of cardiomyocytes. E-Cell System: Basic Concepts and Applications. Landes Bioscience.

54. Ma, D., H. Wei, …, R. Liew. 2013. Generation of patient-specific induced pluripotent stem cell-derived cardiomyocytes as a cellular model of arrhythmogenic right ventricular cardiomyopathy. *Eur. Heart J.* 34:1122–1133.

55. Scheel, O., S. Frech, …, T. Knott. 2014. Action potential characterization of human induced pluripotent stem cell-derived cardiomyocytes using automated patch-clamp technology. *Assay Drug Dev. Technol.* 12:457–469.

56. Lian, X., X. Bao, …, S. P. Palecek. 2015. Chemically defined, albumin-free human cardiomyocyte generation. *Nat. Methods.* 12:595–596.

57. Cohen, A. E., and V. Venkatachalam. 2014. Bringing bioelectricity to light. *Annu. Rev. Biophys.* 43:211–232.

58. Cohen, A. E., and D. R. Hochbaum. 2014. Measuring membrane voltage with microbial rhodopsins. *Methods Mol. Biol.* 1071:97–108.

59. Hou, J. H., V. Venkatachalam, and A. E. Cohen. 2014. Temporal dynamics of microbial rhodopsin fluorescence reports absolute membrane voltage. *Biophys. J.* 106:639–648.

60. Sakai, S., K. Ueno, …, H. Yawo. 2013. Parallel and patterned optogenetic manipulation of neurons in the brain slice using a DMD-based projector. *Neurosci. Res.* 75:59–64.

61. Mattis, J., K. M. Tye, …, K. Deisseroth. 2011. Principles for applying optogenetic tools derived from direct comparative analysis of microbial opsins. *Nat. Methods.* 9:159–172.

62. Govorunova, E. G., O. A. Sineshchekov, …, J. L. Spudich. 2015. NEUROSCIENCE. Natural light-gated anion channels: a family of microbial rhodopsins for advanced optogenetics. *Science.* 349:647–650.

63. Cosentino, C., L. Alberio, …, A. Moroni. 2015. Optogenetics. Engineering of a light-gated potassium channel. *Science.* 348:707–710.

64. Ambrosi, C. M., A. Klimas, …, E. Entcheva. 2014. Cardiac applications of optogenetics. *Prog. Biophys. Mol. Biol.* 115:294–304.

65. Entcheva, E. 2013. Cardiac optogenetics. *Am. J. Physiol. Heart Circ. Physiol.* 304:H1179–H1191.

66. Clements I. P., D. C. Millard, …, A. Heckerling. 2016. Optogenetic stimulation of multiwell MEA plates for neural and cardiac applications. In Proceedings SPIE 9690, Clinical and Translational Neurophotonics; Neural Imaging and Sensing; and Optogenetics and Optical Manipulation. https://doi.org/10.1117/12.2213708.

Biophysical Journal, Volume *115*

Supplemental Information

Light-Activated Dynamic Clamp Using iPSC-Derived Cardiomyocytes

Bonnie Quach, Trine Krogh-Madsen, Emilia Entcheva, and David J. Christini

SUPPORTING MATERIAL

for

Optical dynamic clamp using iPSC-derived cardiomyocytes

by

Bonnie Quach, Trine Krogh-Madsen, Emilia Entcheva, and David J. Christini

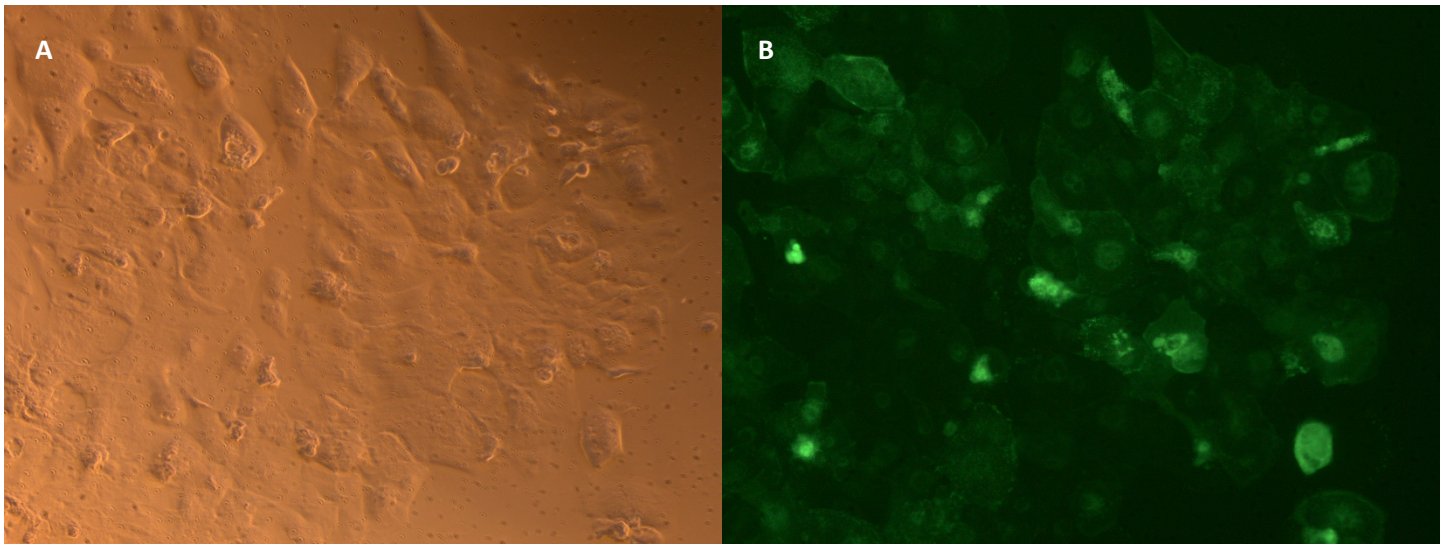

Figure S1: Successful ArchT-eGFP expression in iPSC-CMs

Visualization of eGFP expression following the transfection protocol by Ambrosi and Entcheva (2014).

A) Brightfield image of iPSC-CM beating clusters at 40x.

B) Corresponding image of eGFP fluorescence at 40x.

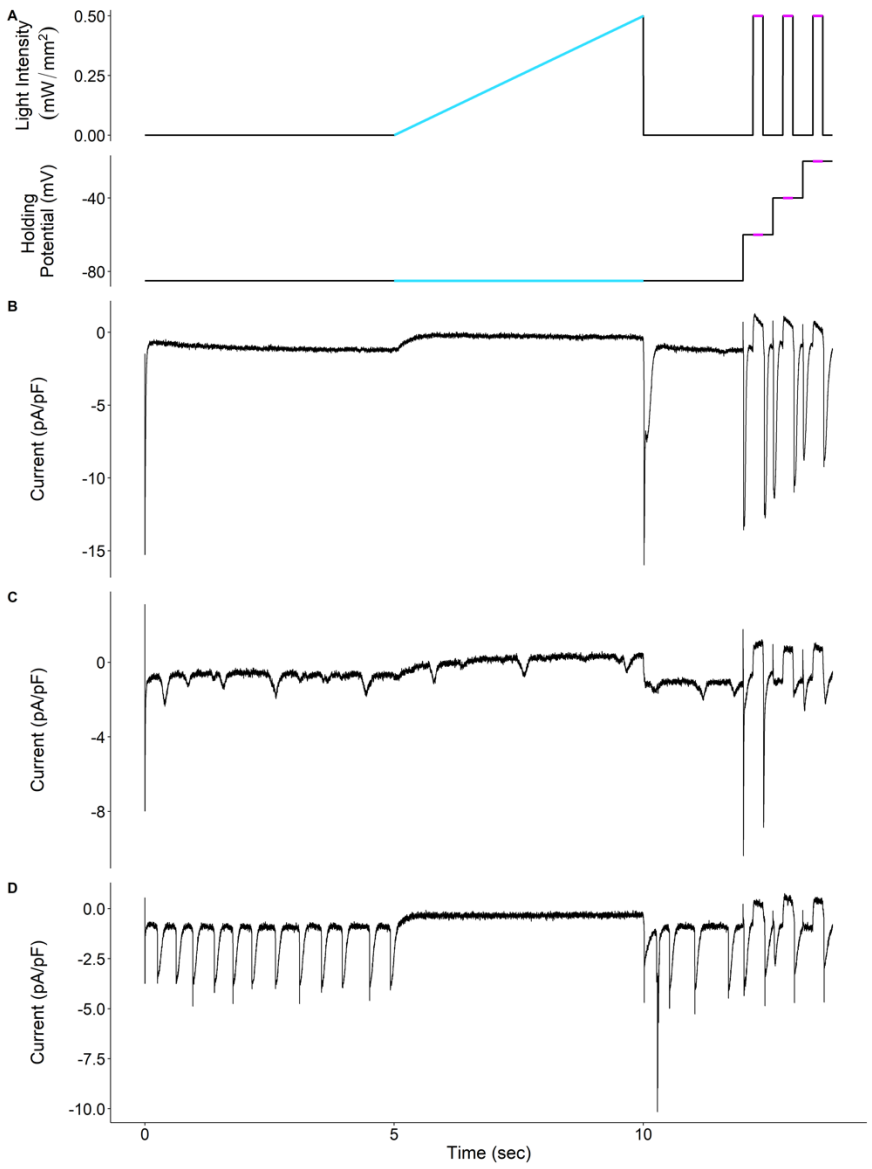

Figure S2: Representative examples of calibration protocol outputs

The calibration protocol (A) can yield a variety of current outputs (B-D) that may be interrupted by repetitive large inward currents (C, D). These inward currents are associated with spontaneous contractions (C, D) which in some cases are suppressed with ArchT activation (D).

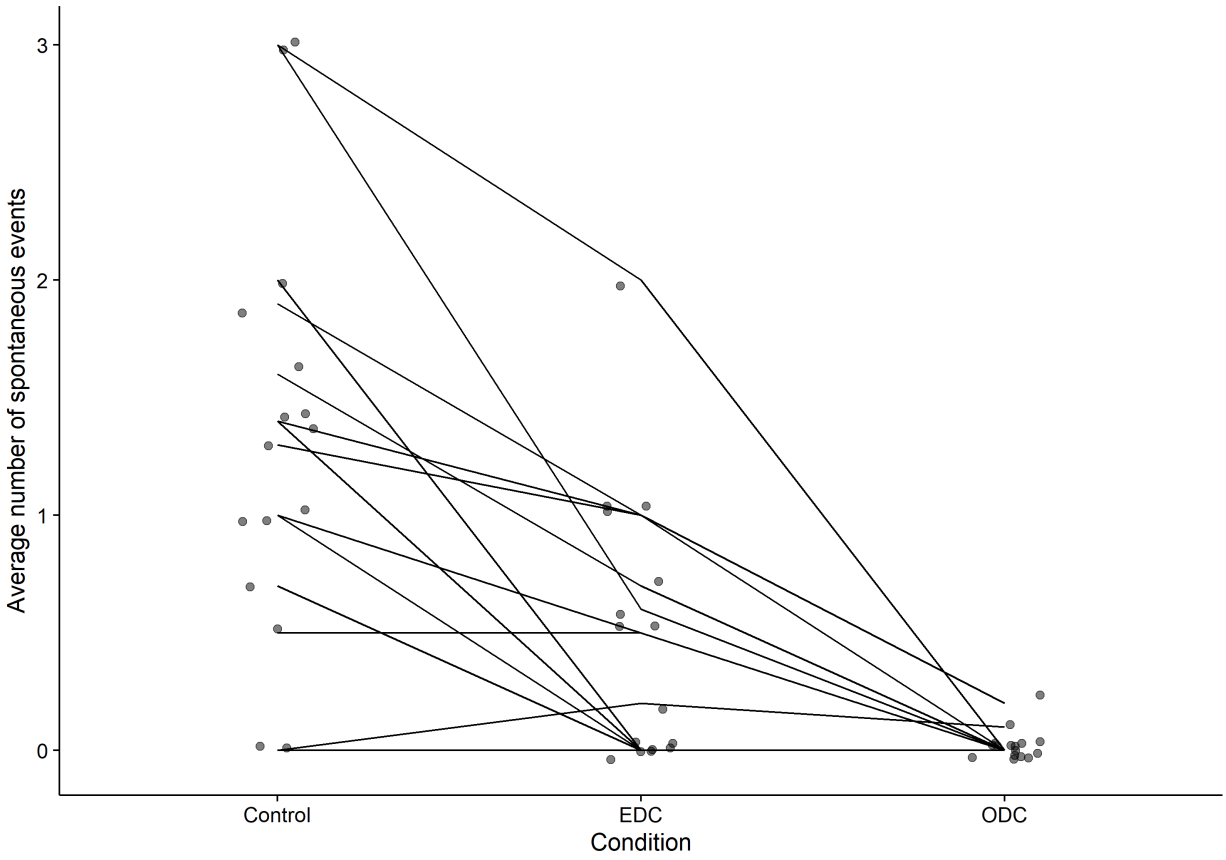

Figure S3: Decrease in spontaneous activity with ODC.

Average number of spontaneous events occurring during sequence of 10 stimulated APs at 0.5 Hz pacing. Each point represents a different cell and the lines connect the results from the same cell.

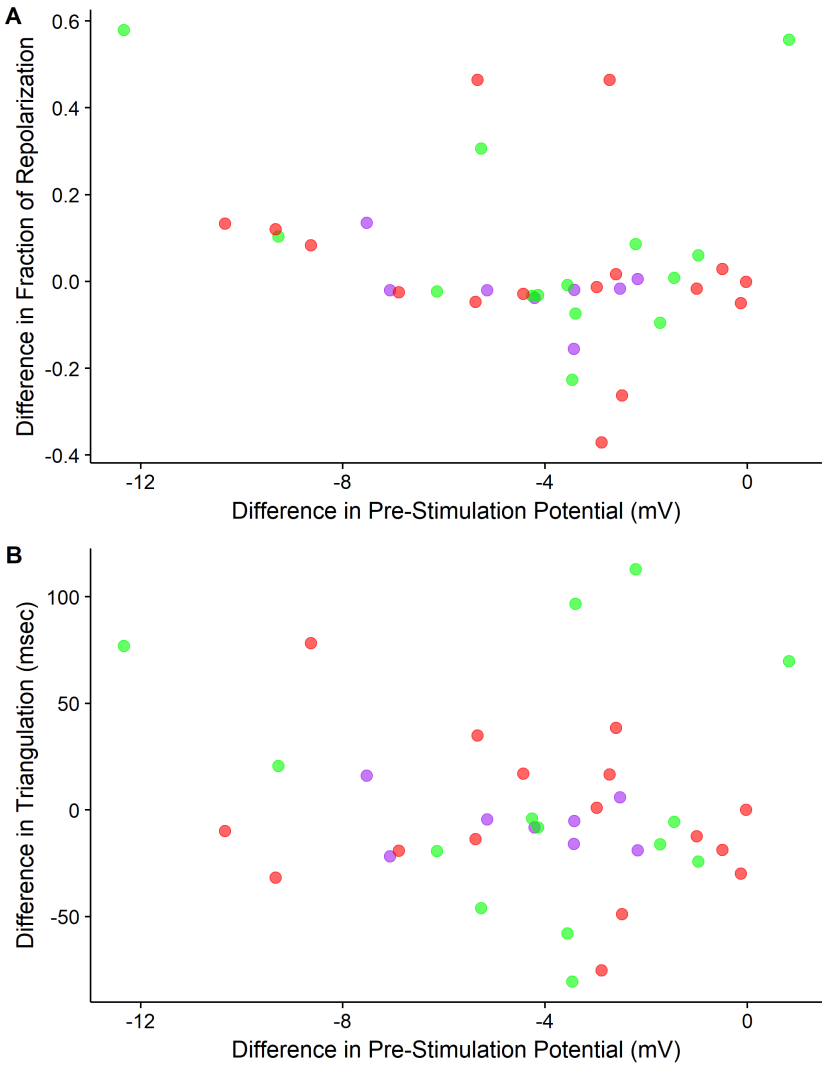

Figure S4: Difference in pre-stimulation potential between EDC and ODC does not correlate with differences in AP morphology characteristics between EDC and ODC

(A) Difference in pre-stimulation potential on difference in fraction of repolarization time. Results at 0.5 Hz, 1 Hz and 2Hz pacing are purple, green, and red, respectively.

(B) Difference in pre-stimulation potential on difference in triangulation. Results at 0.5 Hz, 1 Hz and 2Hz pacing are purple, green, and red, respectively.

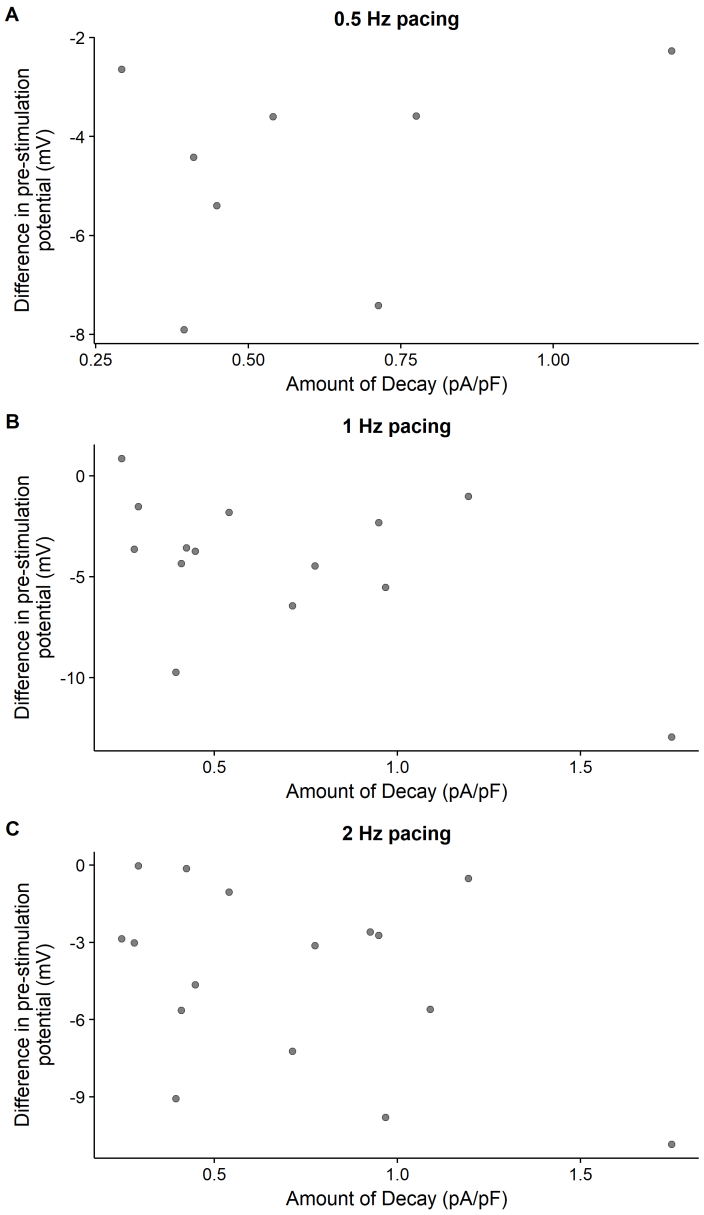

Figure S5: Amount of current decay during constant-intensity light pulses does not correlate with the difference in pre-stimulation potential between EDC and ODC

The amount of current decay was measured as an average difference between the initial current and the final current during the three constant-intensity (0.5 mW/mm^2) light pulses during the calibration protocol. The amount of current decay was compared to the average difference in pre-stimulation potential (mV) between EDC and ODC at (A) 0.5 Hz, (B) 1 Hz, and (C) 2 Hz. Each point represents a different cell.

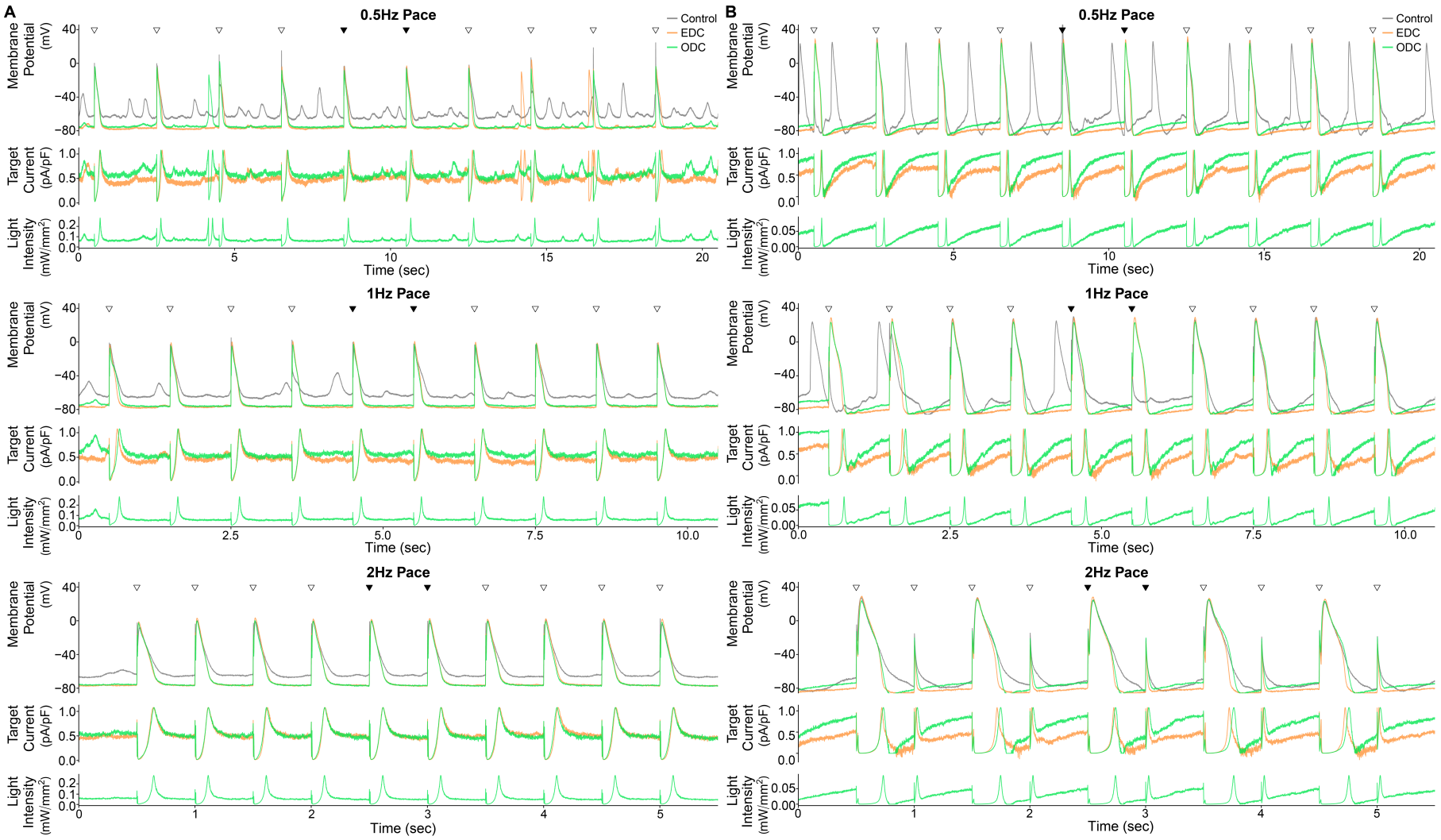
A
B
0.5Hz Pace
1Hz Pace
2Hz Pace
Control
EDC
ODC
Membrane Potential (mV)
Target Current (pA/pF)
Light Intensity (mW/mm²)
Time (sec)

Figure S6: Entire trace of 10 paced APs demonstrating the results of the EDC and ODC platforms from example cells

Results from example cell 1 (A) and cell 10 (B) showing the effects of adding I_{K1} while paced 10 times at 3 different frequencies: 0.5 Hz (top), 1 Hz (middle), 2Hz (bottom). The gray, orange and green traces represent the control without any current addition, adding I_{target} with EDC, and adding I_{target} with ODC, respectively. For each pacing rate, the top panel overlays the 10 paced AP traces over time under control and both dynamic-clamp conditions, and the black triangles indicate when a stimulus current was delivered. In the middle panel, the traces give the calculated target currents for EDC and ODC. The bottom panel shows the calculated light intensity used to generate the target current. The filled black triangles indicate when a stimulus current was delivered and provides a reference to which of the 10 paced APs in Figures 3 (A) and 4 (B) are displayed.

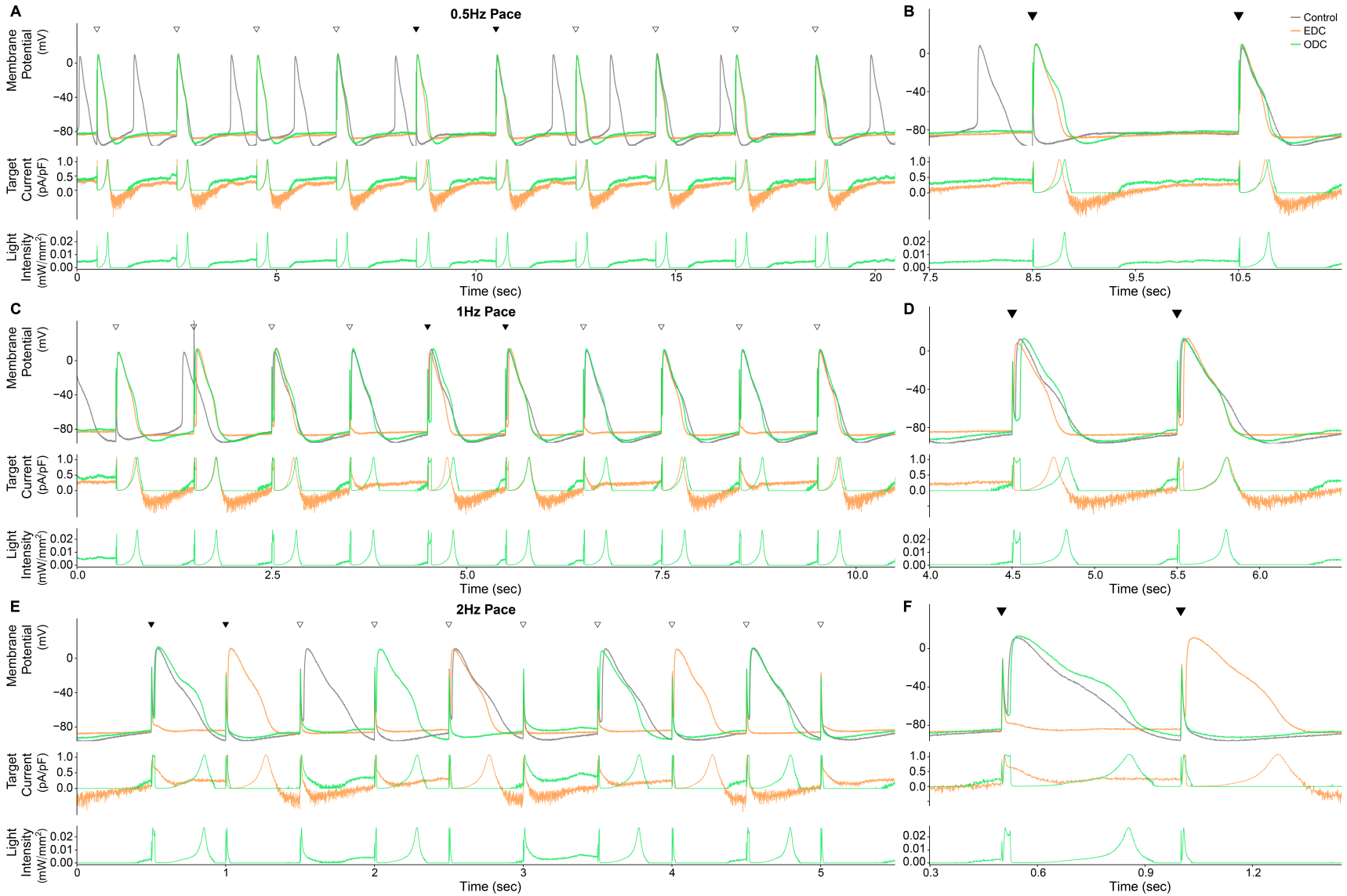
A
0.5Hz Pace
B
Control
EDC
ODC
C
1Hz Pace
D
E
2Hz Pace
F
Membrane Potential (mV)
Target Current (pA/pF)
Light Intensity (mW/mm²)
Time (sec)

Figure S7: Representative example of a large undershoot after an AP and how EDC is able to compensate for the undershoot

Example cell (cell 3) showing the effects of adding I_{K1} while paced 10 times at 3 different frequencies: (A, B) 0.5 Hz, (C, D) 1 Hz, (E, F) 2Hz. The gray, orange and green traces represent the control without any current addition, adding I_{target} with EDC, and adding I_{target} with ODC, respectively. The top panels overlay the 10 paced AP traces under control and both dynamic-clamp conditions, and the black triangles indicate when a stimulus current was delivered. In the middle panels, the traces give the calculated target currents for EDC and ODC. The bottom panels show the calculated light intensity used to generate the target current with ODC. The filled black triangles in the top panels (A, C, E) provide a reference for zoomed portions shown in B, D, and F, respectively.

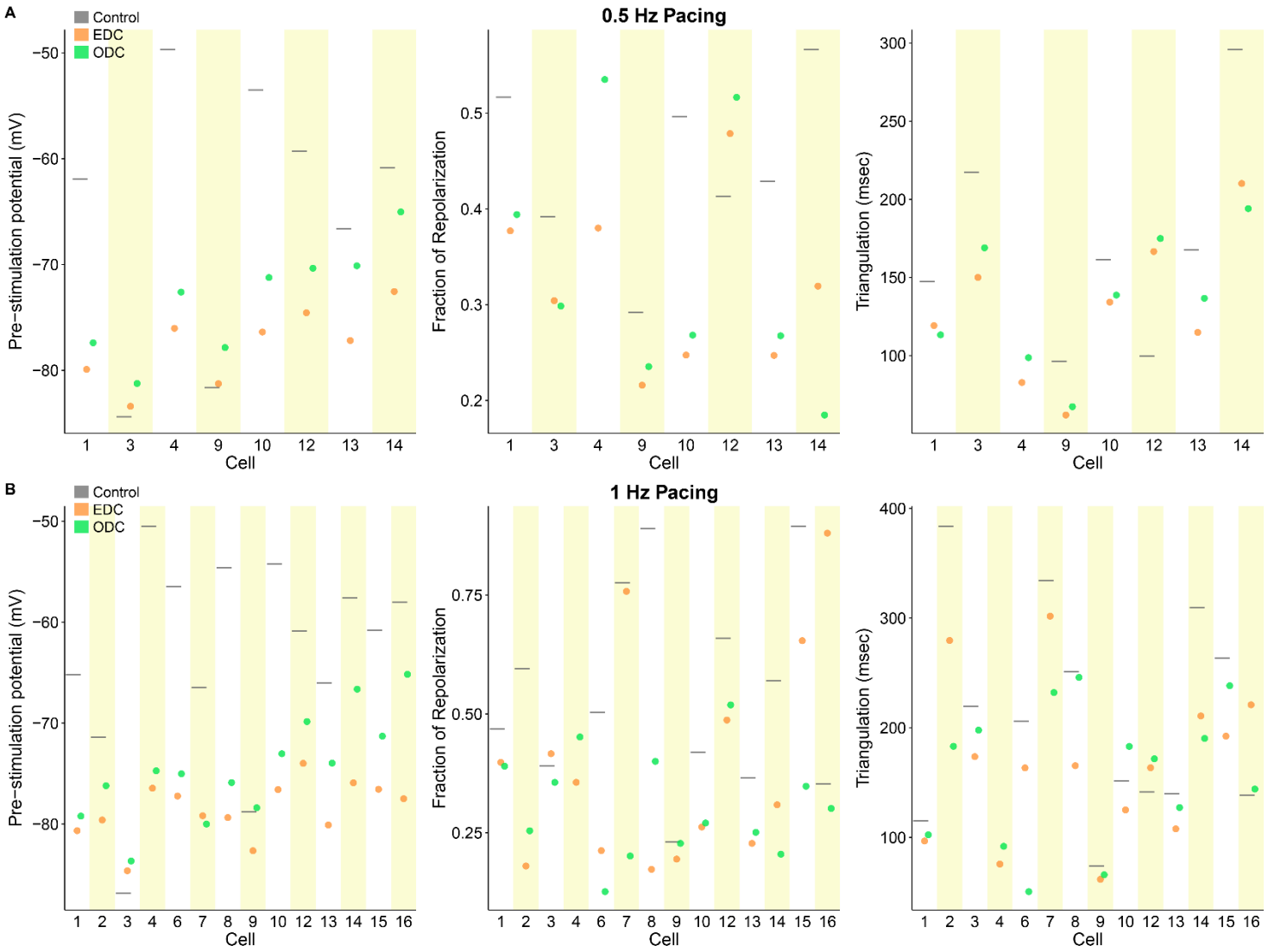

Figure S8: Summary of the effects of EDC or ODC on AP morphology at different pacing frequencies

Pre-stimulation potential (left), fraction of repolarization (middle) and triangulation (right) of individual cells at 0.5 Hz (A) and 1 Hz (B) pacing in control (gray) and after adding an I_{K1} target current via EDC (orange) or ODC (green).

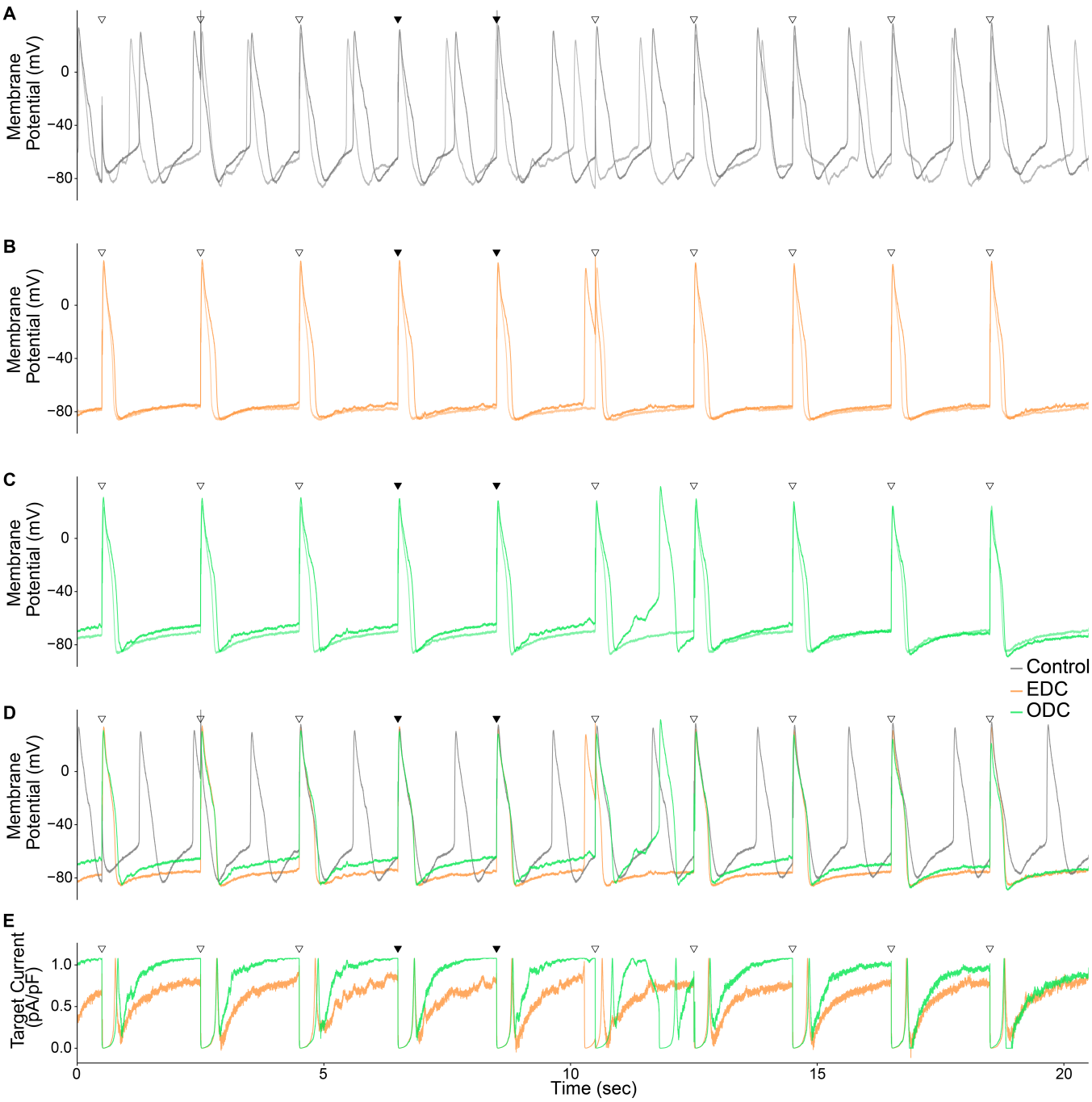

Figure S9: Entire trace of 10 paced APs demonstrating the results of the EDC and ODC platforms from example cell with E-4031 addition

Results from example cell 13 showing the effects of adding I_{K1} while paced 10 times at 0.5 Hz. The figure is organized in the same manner as Figure S6.

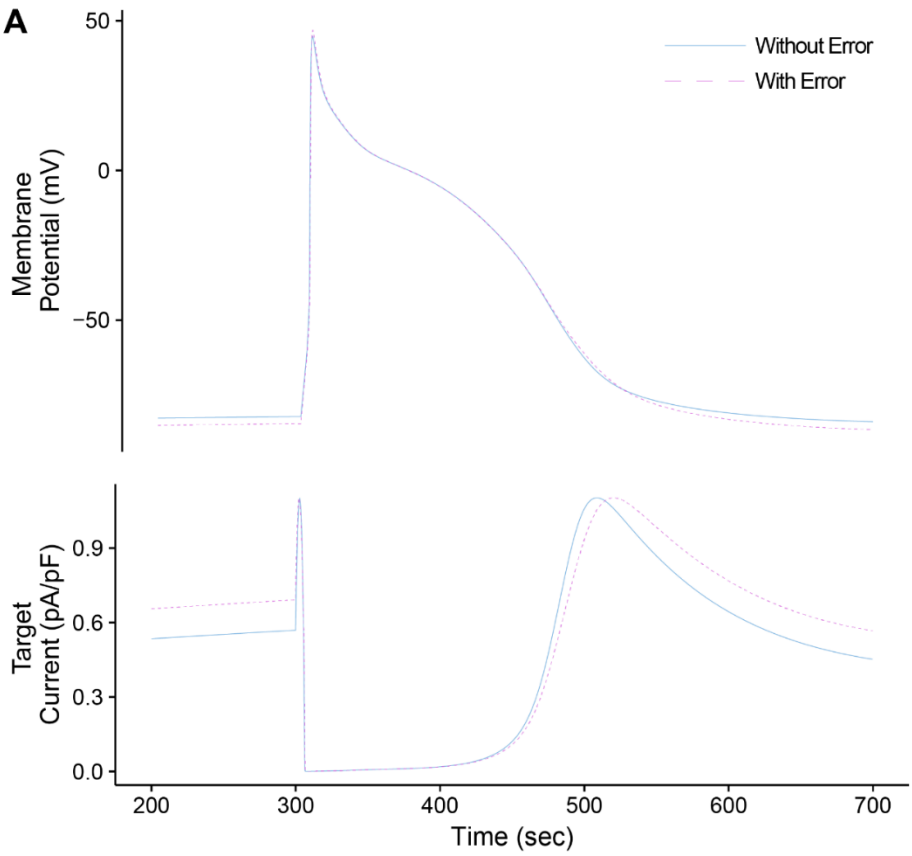

B

	Without Error	With Error
Pre−Stimulation Potential (mV)	−82.4	−84.7
APD_{90} (msec)	214.4	221.9

Figure S10: *In silico* model prediction shows that the error between RTXI and the amplifier has limited impact on dynamic clamp experiments

To predict the effects on dynamic clamp performance of the 5% error between the membrane potential measured by the amplifier versus the membrane potential reported by RTXI, we used an *in silico* approach, simulating I_{K1} dynamic clamp injection into an iPSC-CM computational model (Paci et al., (2013)). We used the same equations for I_{K1} as in our experiments and clamped intracellular [Na^+] to mimic a patched cell. The dynamically clamped iPSC-CM model was run for 810 beats at a 1 Hz pacing rate with and without the amplifier calibration error and the last 10 APs were analyzed. (A) The top panel illustrates the last AP waveform with (dashed purple trace) and without (blue trace) the error. The

bottom panel shows the corresponding target I_{K1}. The presence of the calibration error leads to an overestimation of this current during phase 4 of the AP, causing a small (about 2 mV) hyperpolarization of the resting membrane potential. (B) The resulting AP characteristics with and without the calibration error are very close, with about a 3% change in APD_{90}. Importantly, the predicted effect of the calibration error calculated here does not depend on how the dynamic clamp target current is added to the cell and is therefore expected to affect I_{target} calculated by the EDC and ODC systems equally.

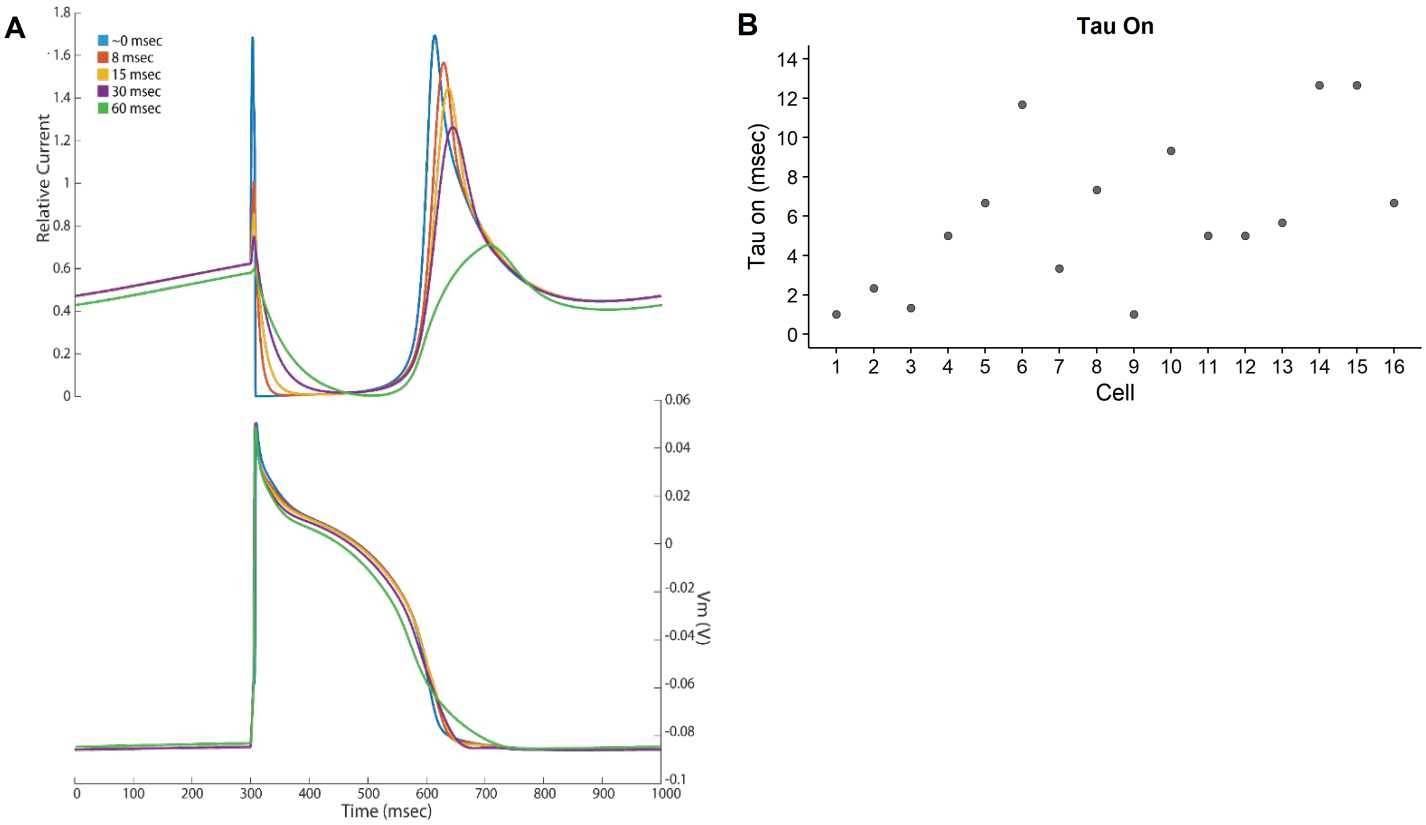

Figure S11: *In silico* model predicting the effect of activation and deactivation kinetics on dynamic clamp performance and experimentally measured ArchT time constants

(A) To test that the kinetics of ArchT are not prohibitively slow for dynamic clamp, we simulated our ODC platform using the Paci et al. (2013) iPSC-CM model with an added ArchT model having a single time constant for activation and deactivation. We varied this time constant to see how large of a delay could be tolerated. The ArchT current generated with different time constants are displayed in the panel above and sthe resulting stimulated APs are in the panel below.

(B) Experimentally measured time constants of activation of ArchT in each cell.

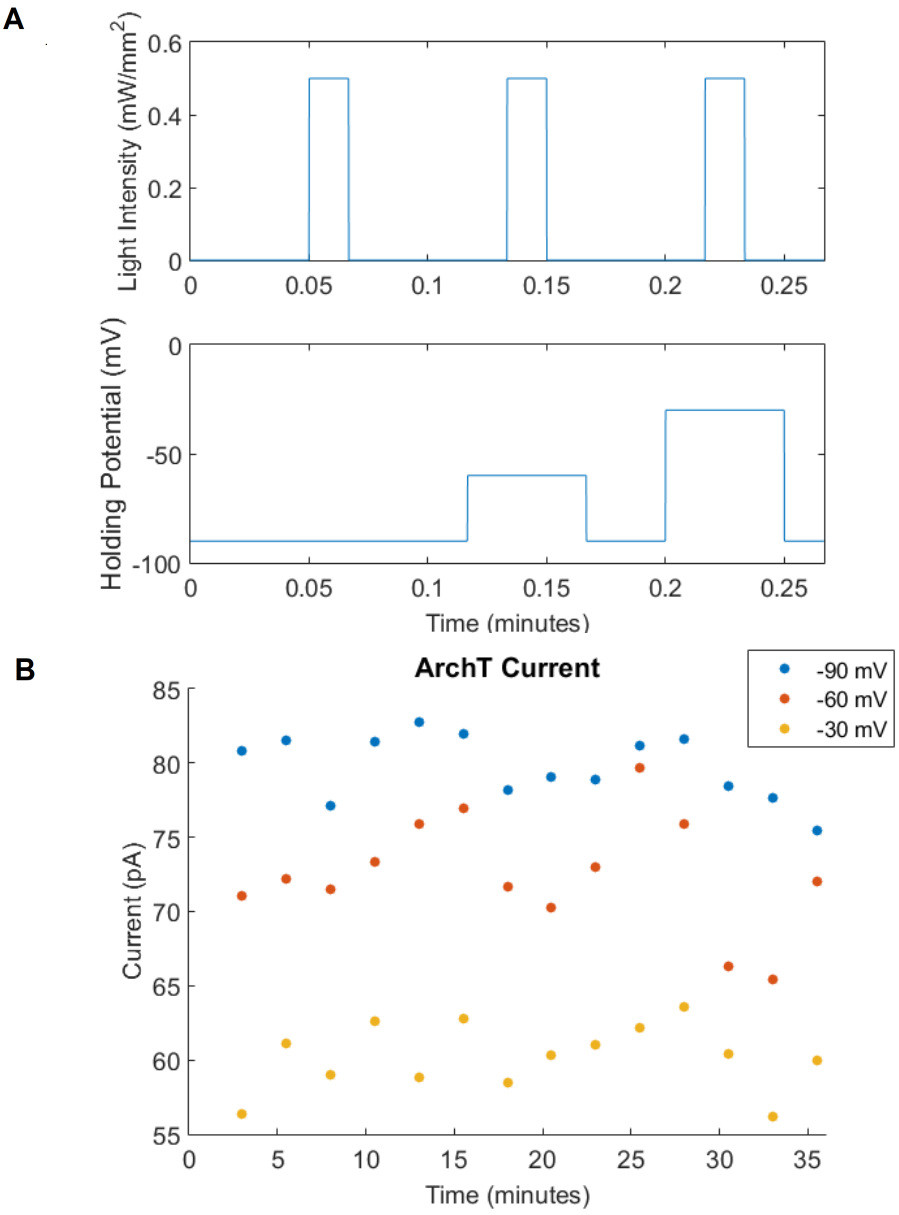

Figure S12: Measuring stability of ArchT illumination during a voltage clamp and light clamp protocol

(A) The top panel shows the light clamp protocol and the bottom panel shows the voltage clamp protocol. This protocol was cycled through repeatedly to measure I_{ArchT} over time and at different holding potentials

(B) Results from a representative cell showing I_{ArchT} produced at different times of the protocol and at different holding potentials.

	PSP			Overshoot			APD_{90}		
	Control	EDC	ODC	Control	EDC	ODC	Control	EDC	ODC
2Hz	-64.9 ± 2.5	-78.3 ± 0.7	-74.2 ± 1.3	22.5 ± 2.9	21.5 ± 2.4	15.4 ± 2.3	265.3 ± 17.7	251.8 ± 17.5	267.0 ± 18.5
1 Hz	-63.2 ± 2.7	-78.6 ± 0.8	-74.5 ± 1.4	21.6 ± 3.4	21.1 ± 5.6	14.6 ± 2.5	269.9 ± 22.4	259.6 ± 20.7	261.7 ± 19.9
0.5 Hz	-64.6 ± 4.4	-77.7 ± 1.3	-73.2 ± 1.9	18.3 ± 4.9	14.8 ± 5.2	11.6 ± 3.8	254.1 ± 30.1	235.2 ± 24.9	241.0 ± 28.1
E4031	-64.1 ± 4.6	-75.8 ± 1.4	-71.1 ± 2.3	7.8 ± 7.3	16.7 ± 6.3	16.4 ± 5.3	711.6 ± 215.8	448.2 ± 98.3	483.6 ± 103.1

Table S1: AP morphology characteristics

The average and SEM of pre-stimulation potential (PSP) (mV), overshoot (mV), and APD_{90} (msec) without dynamic clamp, with EDC and with ODC. The characteristics after E-4031 addition are also listed.